DEVELOPING A COMPTON POLARIMETER TO MEASURE POLARIZATION OF HARD X-RAYS IN THE 50-300 KeV ENERGY RANGE

BY

JASON LEGERE

B.A. in Physics, University of Southern Maine, 2003

THESIS

Submitted to the University of New Hampshire
in Partial Fulfillment of
the Requirements for the Degree of

Master of Science
in
Physics

December, 2005

This thesis has been examined and approved.

Thesis Director, Dr. Mark L. McConnell
Associate Professor of Physics

Dr. James M. Ryan
Professor of Physics

Dr. Per Berglund
Assistant Professor of Physics

Date

DEDICATION

To My Family

ACKNOWLEDGEMENTS

I would like to thank the members of my committee, Mark McConnell, James Ryan, and Per Berglund, for all of their support. Thanks again to my advisor, Mark McConnell, for a job well done. I would also like to thank John Macri for always being available for assistance in the lab. I've learned a great deal about detector/instrumentation development under his guidance. For the simulation work done for SM2 and SM3, I would like to thank Peter Bloser and Tomohiko Narita. I also extend thanks to everyone who has contributed to the development of GRAPE not previously mentioned to include: Mark Widholm, Paul Vachon, and Matt Orr.

This work is currently supported by NASA grants NNG04GB83G and NNG04WC16G.

TABLE OF CONTENTS

DEDICATION……iii

ACKNOWLEDGEMENTS……iv

LIST OF FIGURES……..…viii

ABSTRACT……...……xi

CHAPTER PAGE

INTRODUCTION……..……..……...1

I. SCIENTIFIC BACKGOUND…….....4

A. Emission Mechanisms……..….4

a. Magneto-Bremsstrahlung Radiation……..……..……4

b. Bremsstrahlung Radiation…….…….….6

c. Compton Scattering…….…….…...6

d. Magnetic Photon Splitting……..…….....7

B. Solar Flares…….…….....8

C. Gamma Ray Bursts…….……..…..9

II. COMPTON POLARIMETRY……...……..13

III. THE GRAPE CONCEPT……...……19

A. Initial Concept……..…...…….19

B. Principles of Operation……...……..19

C. GRAPE History……..…….21

a. Science Model 1 (PSPMT Design)……21

D. An Improved Design……..…….24

a. MAPMT Design…….24

b. Science Model 2 (SM2)…….26

c. Science Model 3 (SM3)…….27

IV. SCIENCE MODEL 2 RESULTS…….……29

A. Experimental Setup……..……..29

B. SM2 Data Acquisition……..……..30

C. SM2 Software……..34

a. Data Processing……34

D. Energy Calibrations……..……...35

a. SM2 Calibrations…….……...36

E. SM2 Results…....……...…….40

V. SCIENCE MODEL 3 RESULTS……..…….42

A. Hardware……..……...42

a. SM3 Hardware…….……...42

B. SM3 Software……..……47

C. SM3 Calibrations……..48

D. SM3 Results……..53

a. Simulations…….55

E. Further SM3 Testing……..……..56

VI. FUTURE OF GRAPE……..…….59

A. Science Model 4 (SM4)……...……59

B. GRAPE Deployment…….60

VII. CONCLUSIONS……...……62

LIST OF REFERENCES……...……...63

LIST OF FIGURES

Figure 1: Schematic of GRB model showing the jets and resulting internal and external shocks……..10

Figure 2: The geometrical setup used for cross section equations……14

Figure 3: The basic detector design for a Compton polarimeter…….....16

Figure 4: The modulation pattern observed when Compton scattering polarized radiation with θ = 90°……...…….16

Figure 5: The SM1 design concept……22

Figure 6: The SM1 detector with the PSPMT (left), the plastic scintillator array (middle), and the calorimeter assembly(right).……..……..…….…22

Figure 7: Laboratory polarimeter data showing how the measured data is corrected for intrinsic effects to extract the true modulation pattern…….23

Figure 8: Results from SM1 showing the 90° shift in the modulation pattern…….….24

Figure 9: The MAPMT design concept with 60 plastics surrounding a central CsI(Na) crystal…….……..24

Figure10: The Hamamatsu H8500 MAPMT (top), and several plastic scintillator elements (bottom).……...…..25

Figure 11: SM2 in the initial phase with large plastics populating four anodes for a total of 12 scattering elements……...27

Figure 12: SM3 fully populated with 60 plastics and central CsI(Na) calorimeter……...28

Figure 13: Experimental setup for GRAPE polarized measurements……...…30

Figure 14: Block diagram for the SM2 electronics……...…...….33

Figure 15: SM2 polarizer calibrations spectra. Backscatter techniques were used for the ^{137}Cs and ^{133}Ba sources while the ^{241}Am was measured directly……....37

Figure 16: Energy vs. Channel plot used to determine polarizer energy calibration…....37

Figure17: SM2 CsI calibration spectra. All four sources are measured directly……...38

Figure 18: Energy vs. Channel plot used to determine CsI energy calibration…….38

Figure 19: SM2 calibration spectra. All three sources are measured directly. This plot represents the calibration for a single plastic……...…..39

Figure 20: Energy vs. Channel plot used to determine plastic energy calibration…….40

Figure 21: Results from SM2 showing the 90° shift in the modulation pattern when rotating the detector 90° to the incident polarization vector……....41

Figure 22: The preamp circuit boards plugged into the back end of the MAPMT……...43

Figure 23: GRAPE setup for SM3 using the VME crate housing the ADCs and CFD….46

Figure 24: SM3 polarizer calibrations spectra. Backscatter techniques were used for the ^{137}Cs and ^{133}Ba sources while the ^{241}Am was measured directly.……...49

Figure 25: Energy vs. Channel plot used to determine polarizer energy calibration...….49

Figure 26: SM3 CsI calibration spectra. All four sources are measured directly ……..…50

Figure 27: Energy vs. Channel plot used to determine CsI energy calibration…….....50

Figure 28: Schematic showing the setup for backscatter calibration…….……51

Figure29: SM3 plastic calibration spectrum for a single plastic. Backscatter techniques were used to measure ^{57}Co……...…52

Figure 30: SM3 plastic calibration spectrum for a single plastic. Backscatter techniques were used to measure ^{133}Ba……..52

Figure 31: Energy vs. Channel plot used to determine plastic energy calibration……....53

Figure 32: Cut away schematic of the CsI and surrounding plastics…….54

Figure 33:Results from SM3 with inner plastic ring eliminated……...….55

Figure 34:MGEANT simulated polarimeter experiment of SM3…….....….56

Figure 35: SM3 results using the ^{137}Cs source scattered through 120°…….....….57

Figure 36: Simulated results showing the improved energy resolution of the SM4 design that would result from changing the CsI calorimeter to one made from $LaBr_3$……..…59

Figure 37: An array of four GRAPE modules…….....61

ABSTRACT

DEVELOPING A COMPTON POLARIMETER TO MEASURE POLARIZATION OF HARD X-RAYS IN THE 50-300 KeV ENERGY RANGE

By

Jason Legere

University of New Hampshire, December 2005

We describe the development of GRAPE (Gamma-Ray Polarimeter Experiment), a hard X-ray Compton Polarimeter. The purpose of GRAPE is to measure the polarization of hard X-rays from astronomical sources in the 50-300 keV energy range. We are particularly interested in X-rays that are emitted from solar flares and cosmic gamma-ray bursts (GRBs). Accurately measuring the polarization of the emitted radiation from these sources will lead to a better understating of both the emission mechanisms and source geometries. The GRAPE design consists of an array of plastic scintillators surrounding a central high-Z crystal scintillator. The geometry of the photon scatters between detector elements provides a means of measuring the linear polarization of the incident photon flux. We can monitor individual Compton scatters that occur in the plastic scintillators. A Compton scattered photon that is subsequently absorbed by the high-Z crystal constitutes a valid event. An analysis of the scatter angles of these valid events produces a distribution that incorporates a signature of the polarization level of the incident radiation. Comparing with Monte Carlo simulations of a 100% polarized beam,

the level of polarization of the measured beam can then be determined. The complete array is mounted on a flat-panel multi-anode photomultiplier tube (MAPMT) that can measure the locations and deposited energies resulting from the photon interactions. The design of the detector provides a large field-of-view (>π steradian). The compact nature of the design permits the close-packing of multiple modules in large-area configurations. This thesis describes the most recent development efforts and the latest laboratory results obtained with a GRAPE science model.

INTRODUCTION

In the study of celestial sources, there are four properties of the source emitted radiation that can be measured; energy, intensity, direction, and polarization. At X-ray energies, many experiments have been conducted to measure the energy, intensity and direction of these incoming photons, but measurements of polarization have been lacking largely due to the lack of instrumentation with sufficient sensitivity. Polarization measurements have become a powerful tool for astronomers throughout much of the electromagnetic spectrum, but polarimetry has yet to be exploited at these high energies. It is believed that by accurately measuring X-ray polarization levels from solar flares and GRBs we will be able to better understand both the emission mechanisms and source geometries producing the radiation [1].

The mechanisms responsible for the emission of gamma rays are mainly non-thermal, many of which can lead to high degrees of linear polarization [1]. Four such mechanisms are 1) magneto-bremsstrahlung radiation, a general classification that includes cyclotron, synchrotron, and curvature radiation; 2) Compton scattering, which can polarize initially unpolarized photons; 3) electron-proton Bremsstrahlung radiation, that can produce levels of linear polarization up to 80%; and 4) magnetic photon splitting, that can lead to polarization levels up to 30%. Each of these mechanisms is characterized by well-known energy-dependent levels of polarization. The observed polarization of a given source will then depend not only on the radiation mechanism(s), but also on the detailed source geometry.

We have developed and tested a Compton polarimeter in the laboratory, known as GRAPE (Gamma-Ray Polarimeter Experiment). The purpose of GRAPE is to measure the polarization of hard X-rays in the 50-300 keV energy range. As described here, the GRAPE design is most suitable for studies of either gamma-ray bursts or solar flares, either on a long-duration balloon platform or a satellite platform.

A solar flare occurs when the magnetic energy builds up in the solar atmosphere and is suddenly released. The process takes place in so-called active regions, regions dominated by magnetic fields. During the energy release, high-energy subatomic particles, mostly electrons, protons and neutrons, are accelerated to very high energies. The ions can be accelerated up to at least tens of GeV and the electrons at least up to hundreds of MeV. The interaction of these accelerated particles with the solar atmosphere generates X-rays and gamma rays. The study of the polarization of these X-rays and gamma rays emitted from solar flares will help in determining the extent to which the accelerated electrons are beamed, which in turn, has important implications for particle acceleration models [2-10].

Another class of object where polarization measurements will be of interest is gamma-ray bursts (GRBs). Being the brightest source of gamma rays known, they are now believed to be located in distant galaxies. These great distances infer that GRBs radiate 10^{51}-10^{53} ergs or more over several seconds. The current model of GRBs is one that describes this release in terms of a relativistic fireball model. According to the fireball model, gamma rays are emitted when an ultra-relativistic $(\gamma \sim 10^4)$ energy flow is converted into radiation via internal shocks [11, 12].

The mechanism of the “inner engine” is of particular interest. There have been numerous models proposed to describe this “inner engine.” Most tend to describe the release as a massive short-lived accretion disk surrounding a black hole with the release of energy along the axis of rotation in the form of jets. For each model it is expected that accurate polarization measurements will give a clearer picture as to the energy release mechanism and the source geometry.

In the following we present a brief scientific background along with a review of Compton polarimetry followed by a brief history of GRAPE and results for previous laboratory science models. We then discuss the current data from the third GRAPE science model. The future of the GRAPE design and possible deployment options are then reviewed.

CHAPTER I

SCIENTIFIC BACKGROUND

Emission Mechanisms

Many models for astrophysical gamma-ray emission involve beams of highly energetic particles in strong magnetic fields. These ordered geometries will also result in the linear polarization of these gamma-rays [1]. The hard X-ray emission from a bremsstrahlung source such as a solar flare will be polarized if the electrons are accelerated anisotropically rather than in a relatively broad angular distribution [26]. Therefore polarization measurements of solar flares can give us an idea as to the extent to which the electrons are beamed, which in turn has important implications for particle acceleration models.

Polarimetric measurements have the ability to provide important constraints for potential source emission mechanisms. By accurately measuring polarization levels of the emitted gamma-rays from solar flares and gamma-ray bursts (GRBs), it may possible to determine both the emission mechanisms and source geometries producing the radiation.

Magneto-Bremsstrahlung Radiation

Magneto-Bremsstrahlung radiation is the radiation emitted when charged particles are accelerated in a magnetic field. It is believed to be an important emission mechanism for many astronomical objects, including pulsars and GRBs. Electrons are the primary

particle causing emission in most astrophysical sources due to their low mass, allowing them to experience much greater accelerations than heavier ions. There are two general cases of magneto-Bremsstrahlung radiation involving electrons. The cyclotron case is a result of non-relativistic electrons while the synchrotron case is a result of ultra-relativistic electrons. A special case of magneto-Bremsstrahlung emission, curvature radiation, results from electrons moving along curved magnetic field lines.

All three cases of magnetic-Bremsstrahlung radiation will produce linear polarization of gamma-rays at predicted levels with a well-defined energy dependence. In the case of cyclotron emission, emitted gamma-rays can be 100% polarized but are limited to energies below ~100 keV. This is due to the immense magnetic field strengths (neutron stars) required to generate photons up to this energy. Depending on the viewing angle of the observer the gamma-rays can be circularly polarized (viewed along the magnetic field line,) elliptically polarized (viewed off-axis from the field lines,) or linearly polarized (viewed perpendicular to the magnetic field line axis.)

For ultra-relativistic electrons, synchrotron emission can produce polarization levels of 80% for gamma-rays with MeV energies. A significant feature of synchrotron emission is that the radiation is beamed in the direction of the electron. This results in a beam that is highly collimated, allowing observations only when the beam sweeps past the observer. The 80% polarization level represents a maximum and any observed radiation will likely be measured lower levels of polarization due to any inhomogeneities in magnetic field structure [1].

Curvature radiation will result if the direction of the magnetic field causes the electron to drift with a small radius of curvature. It must be a sufficiently small radius of

curvature and sufficiently high magnetic fields. Therefore curvature radiation is only significant for magnetized neutron stars (pulsars.) Characteristics of curvature radiation (energies and polarization levels) are similar to synchrotron radiation, except that the observed polarization vector of curvature radiation is parallel to the magnetic field vector [1]. The observed polarization vector in synchrotron radiation will be orthogonal to the magnetic field vector.

Bremsstrahlung Radiation

Bremsstrahlung radiation is the radiation emitted from the acceleration of a charged particle in the electrostatic field of an ion. Again due to their low mass electrons are the primary radiators. Bremsstrahlung radiation is associated with free electrons within a hot gas. The photons emitted tend to be perpendicular to the electron's plane of motion with the polarization vector parallel to the direction of acceleration. The level of linear polarization in gamma-rays resulting from Bremsstrahlung emission is extremely dependent upon the emission angle and can reach levels as high as 75% for 100 keV photons. This angular dependence may prove useful in determining the source geometry, as in the case of solar flares [1]. Bremsstrahlung is the primary emission mechanism for hard (~100keV) X-rays in solar flares. The radiation results from accelerated electrons interacting in the solar atmosphere.

Compton Scattering

Compton scattering is the collision of a photon and an electron resulting in the transfer of energy and momentum. Generally the collision involves a high-energy photon

with a low-energy electron. If the collision involves low-energy photons and relativistic electrons it is often referred to as inverse Compton scattering. Both interactions will result in linearly polarized radiation. The theory behind the polarization process is discussed in detail in chapter two. For incident unpolarized photons, Compton scattering can produce levels of linear polarization reaching 100%. The level of polarization is dependent on the initial photon energy and the scattering angle. As the energy of the initial photon increases the level of polarization drops rapidly to ~48% for 1 MeV photons scattered through ~90°. For a given initial photon energy there exists a scattering angle that results in the maximum polarization level. Any deviation from this optimum angle will results in increasingly lower polarization levels.

Constraining this mechanism is the fact that incident photons must not form an isotropic distribution [1]. If the polarization vectors of the incident photons are not aligned the scattered radiation will contain polarized components from all directions effectively canceling out each other. The result will be an unpolarized distribution. Compton scattering is a possible emission mechanism for GRBs and black holes.

Magnetic Photon Splitting

Another possible emission mechanism of polarized radiation is magnetic photon splitting. In the presence of strong magnetic fields ($>10^{13}$ G), such as neutron stars, incident photons can be split into two photons. These strong magnetic fields suggest neutron stars sources, possibly GRBs, to be likely regions of magnetic photon splitting. The resulting photons can be strongly polarized (20-30%) [1]. An important feature of magnetic photon splitting is the reversal of the polarization angle at the peak of the

emitted spectrum. This energy-dependence can help to identify photon-splitting as a radiation mechanism.

Solar Flares

Solar flares represent a phenomenon where polarization measurements are expected to be useful. Many models of nonthermal hard X-ray emission in solar flares predict a polarization signal with levels > 10% [27-33]. Depending on the polarization of the initial flux in the 20-100 keV range, a certain component of the observed emission will be from backscattered gamma-rays off the photosphere, influencing the degree of polarization of the observed flux. This backscatter component will introduce polarization fractions of a few percent at energies below 100 keV [28, 29]. A thermal component with a low level polarization is also present and tends to dominate the emission from all flares with energies below 25 keV. For these reasons it is argued that polarization measurements are more revealing at higher energy levels (~100 keV and above) [34].

Polarization measurements of solar flares date back to the Soviet Intercosmos satellites. On board polarimeters measured polarization levels of 40%(±20%) at energies of ~15 keV for three small X-ray flares [35]. Three other flares were analyzed during October and November 1970 and showed polarizations of ~20%. Due to the low number of photon statistics and the fact that the experimenters did not allow for detector cross-calibration issues, the results were met with much disbelief. Later observations on the OSO-7 satellite showed polarization levels of ~10%, but unfortunately due to in-flight gain shifts the data were compromised [36]. A later study using Intercosmos 11 indicated polarization levels of only a few percent in the 15 keV range [37]. Another small

polarimeter was flown on an early shuttle mission that measured levels between 2.5% and 12.7% in the 5-20 keV range [38]. Unfortunately contamination of the Li scattering material invalidated the pre-flight calibration. These measurements, if valid, only provide information on the predicted thermal and backscatter component. A need for higher energy analysis still exists to study the non-thermal emission.

Most recently polarization measurements have been conducted of an X4.8-class solar flare on July 23, 2002 using RHESSI [26, 39, 40]. Although primarily designed as an imager, RHESSI is capable of measuring polarization levels extending to ~100 keV [26]. At this energy it may be possible to reject the thermal emission background. Although an improvement on the previous missions, some fraction of the observed hard X-ray flux will still contain a backscatter component. The need for a polarimeter in higher energy ranges is still a much-needed next step.

Gamma Ray Bursts

Gamma-ray bursts (GRBs) were first detected in 1967 by the Vela series of satellites [13]. These satellites were launched in an effort to monitor violations of the nuclear test ban treaty. The Vela satellites were equally spaced in circular orbits, which allowed for the discovery that GRBs were not of solar or terrestrial origin. This was done by using the arrival times of the bursts measured by each satellite to calculate the direction of the GRB.

For more than 20 years, it remained unclear whether GRBs originated within our galaxy or at cosmological distances. Several satellites dedicated to observing GRBs were

launched but were unable to determine their distance due to their inability to quickly determine the GRB location with high precision. In 1997 the question of GRB distance was finally settled during the Beppo-SAX satellite mission. Beppo-SAX was able to measure the X-ray afterglow, and determine the location with high precision [14]. This allowed optical observers to get a spectrum, and it was revealed that they originate at cosmological distances. At these distances GRBs are the brightest source of gamma-rays known to date and the largest energy release since the Big Bang.

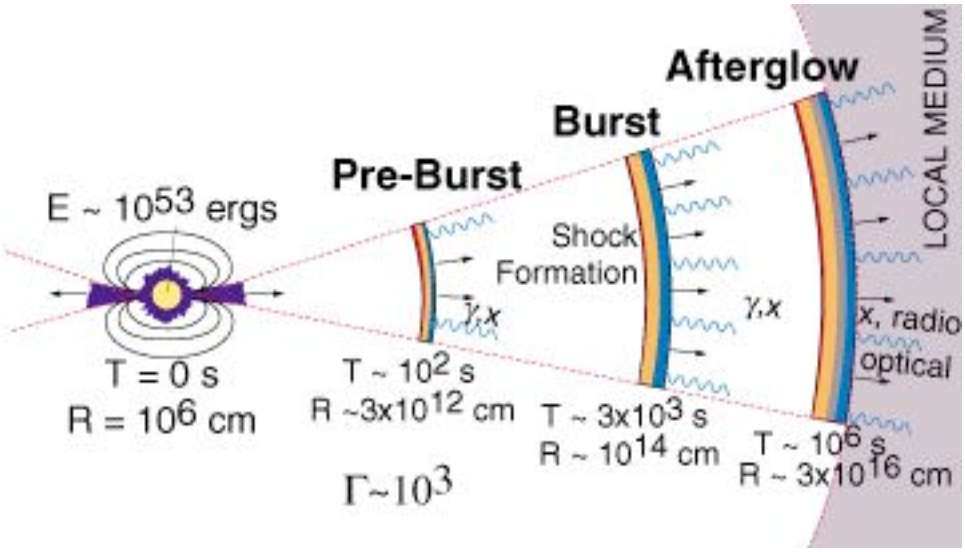

Figure 1: Schematic of GRB model showing the jets and resulting internal and external shocks.

There have been a number of models suggested for GRBs. The greatest difficulty in constructing GRB models stems from their enormous release of energy, 10^{51}-10^{53} ergs. To fully describe the process of a GRB we need to comprehend the initial release of energy, the "inner engine," and the subsequent conversion of energy into radiation. Most models for the "inner engine" are of a gravitational collapse or merger of compact

objects. One model involves the merger between neutron stars or black holes in binary systems [15]. Another model suggests the collapse of a star in a massive supernova ($M>30M_{\odot}$) called a "hypernova" [16, 17]. The common feature of most (if not all) models is that the energy release takes the form of jets directed along the rotational axis of the system, Fig. 1.

The idea of a cosmic fireball is currently used to describe the energy conversion process [11, 12]. According to this picture, gamma-rays are produced by internal shocks within an outgoing ultra-relativistic energy flow. As slower moving shells are overcome by faster moving ones a shock is generated that emits gamma-rays. When the outgoing flow reaches the local interstellar material it is believed that the longer wavelength afterglow emission is created from the resulting ("external") shocks. The nature of the "inner engine" that this energy outflow arises from is still under speculation.

Polarization measurements have a potential to tell us something about both the radiation mechanisms and the geometry of the energy outflows. There have been optical studies of the polarization of GRB afterglows. Observed polarization levels of ~10% in several GRBs have provided direct evidence for geometrical beaming of emission in the external shocks [18-20]. These studies only observe the external shock and therefore are insensitive to the nature of the "inner engine." The measurement of the prompt gamma-ray emission is therefore required to similarly probe the internal shock region. If the flow of emission is a result of synchrotron emission in a continuously spreading jet, it is expected that a somewhat higher level of polarization (>20%) could be present in the gamma-ray emission [21-24].

Recent measurements using RHESSI as a polarimeter have suggested a very high (much disputed) level of polarization (80%) at energies between 150 keV and 2 MeV for GRB021206 [25]. This high level of polarization suggests a synchrotron origin for the emission, implying that the engine driving the GRBs has a strong, large-scale magnetic field. Another potential mechanism for polarization is induced Compton scattering. If unpolarized gamma-rays are beamed into a small angle jet and Compton scattered at an angle θ into our line of sight, polarization levels could reach upwards of 70% [25]. Initially unpolarized gamma-rays would be required to have a large initial energy. In addition they must undergo only a single scatter in our direction otherwise secondary scatters would erase the original induced polarization. Although the Compton scattering component may exist, the process is inefficient and requires a much higher initial energy and luminosity. This tends to favor the synchrotron case. This result, indicating very high levels of polarization, points to the potential for gamma-ray polarization measurements of GRBs.

CHAPTER II

COMPTON POLARIMETRY

Measuring the polarization of X-rays in the 50-300 keV energy range is most easily done by taking advantage of the Compton scattering mechanism. For an incident photon with frequency ν_0 the Compton scattering differential cross section is given by the Klein-Nishina formula,

$$\frac{d\sigma}{d\Omega} = \frac{{r_o}^2}{2}\left(\frac{\nu'}{\nu_o}\right)^2\left(\frac{\nu_o}{\nu'} + \frac{\nu'}{\nu_o} - 2\sin^2\theta\cos^2\eta\right) \tag{1}$$

where,

$$\frac{\nu'}{\nu_o} = \frac{1}{1 + \left(\frac{h\nu_o}{mc^2}\right)\left(1 - \cos\theta\right)} \tag{2}$$

with ν' the frequency of the scattered photon. The angle θ is the Compton scattering angle of the scattered photon measured from the direction of the incident photon, and η is the azimuthal angle of the scattered photon measured in the plane containing the electric field vector (E_O) of the incident photon (Fig. 2.)

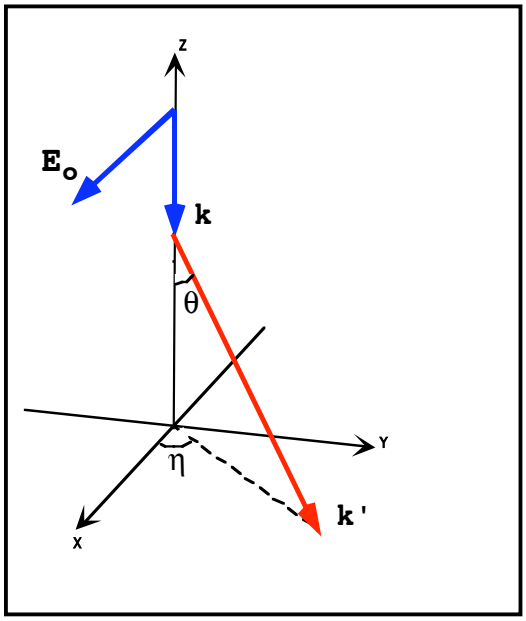

Figure 2: The geometrical setup used for cross section equations.

Investigating Equation 1 we can see that for a fixed value of θ the scattering cross section for polarized photons is a maximum at η = 90° and a minimum at η = 0°. This leads to an asymmetry in the number of photons scattered in the direction parallel and orthogonal to the incident photon electric vector. In other words, photons will tend to scatter at 90° with respect to the incident electric field vector. It is this asymmetry that is utilized in the Compton polarimeter.

The basic design of a Compton polarimeter is one that consists of two detectors (Fig. 3) [1, 41]. One detector acts as a medium for the Compton interaction (detector A), while the other serves as a calorimeter to absorb the scattered photon (detector B.) Collectively the detectors are capable of determining the energies of the scattered photon and recoil electron along with the location of the Compton interaction site and direction of the scattered photon. Detector A, a low-Z (scattering) detector, has a high probability

of Compton interactions, and detector B, a high-Z detector (calorimeter) that has a high probability of absorbing the scattered photon. By analyzing the kinematics of each event we can determine the path of each scattered photon within the polarimeter. The polarization measurement is accomplished by recording the azimuthal modulation pattern of the scattered photons (Fig. 4.) We bin each valid scattering event by its corresponding azimuthal scattering angle. The measured distribution is then corrected using an unpolarized distribution measured in the lab or simulated. This corrects for instrumental asymmetries and/or associated geometric effects that are design specific. A modulation pattern is produced that can be fit with,

$$C(\eta) = A\cos\left(2\left(\eta - \varphi + \frac{\pi}{2}\right)\right) + B \tag{3}$$

where φ is the polarization angle of the incident photons and A and B are constants used in the fit. With a proper modulation fit we can use the parameters A and B to find the polarization modulation factor μ_p.

$$\mu_p = \frac{C_{p,\max} - C_{p,\min}}{C_{p,\max} + C_{p,\min}} = \frac{A}{B} \tag{4}$$

$C_{p,\max}$ and $C_{p,\min}$ represent the maximum and minimum number of counts measured in the polarimeter, Fig 4 [1, 42].

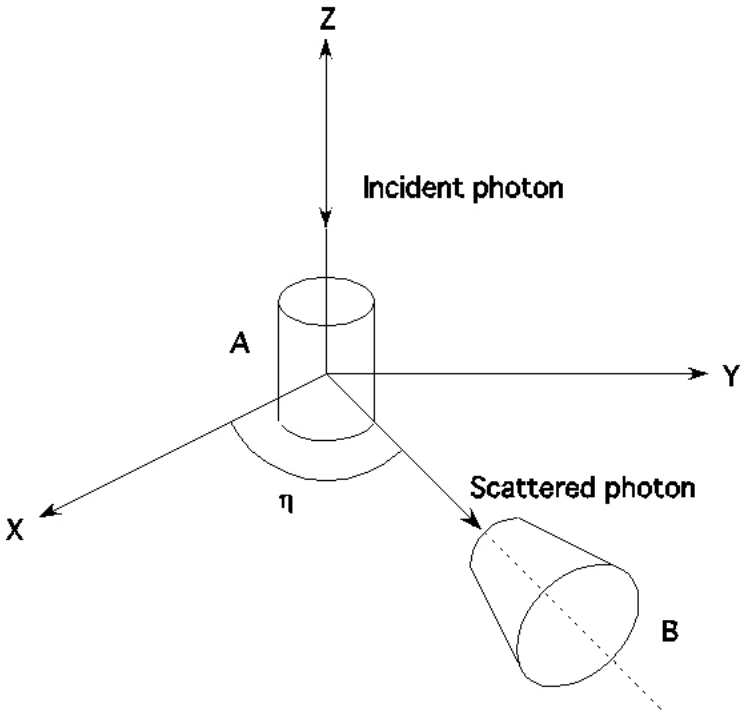

Figure 3: The Basic detector design for a Compton polarimeter. This design rotates the absorbing detector about η with the scattering detector fixed. Detector B absorbs the scattered photon and also records η.

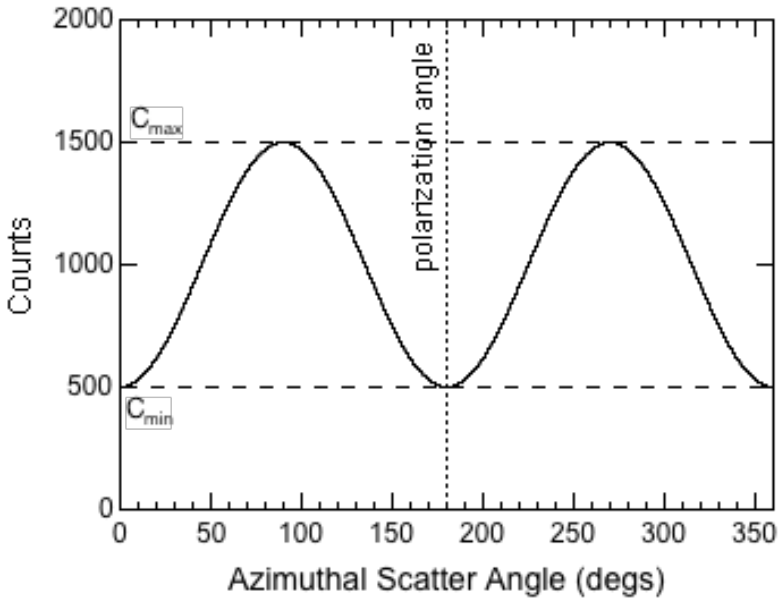

Figure 4: The modulation pattern observed when Compton scattering polarized radiation with θ = 90°.

The quality of the polarization signature is quantified by the polarization modulation factor. In order to maximize the modulation factor the detector geometry needs to be considered, particularly the scattering angle θ. This if found by plugging $d\sigma(\eta = 90)$ and $d\sigma(\eta = 0)$ for $C_{p,\max}$ and $C_{p,\min}$, respectively, into equation 4. The result is

$$\mu_p = \frac{\sin^2\theta}{\varepsilon^{-1} + \varepsilon - \sin^2\theta} \tag{5}$$

When equation 5 is plotted for various incident photon energies and scattering angles it is discovered that in the 50-300 keV energy range an approximately 90° scattering angle (θ) will result in the maximum modulation factor.

The figure-of-merit for a given detector design is obtained using μ_{100}, the modulation factor for 100% polarized incident photons. This can be measured experimentally or by performing Monte Carlo simulations for the particular detector design and structure. Our current simulations use the GEANT3 code from CERN. In order to simulate the polarized photons we use the GLEPS extension of the GLECS package. The GLECS package program is an extension of the GEANT3 simulation package, which allows for the simulation of the detailed physics involved with Compton and Rayleigh scattering. The GLEPS extension was developed to include the effects of polarized incident photons for the Compton and Rayleigh processes [43]. By running the simulations using the GLEPS extension we are able to accurately simulate the response

of a particular detector design to 100% polarized photons obtaining μ_{100}. The simulations included all important components of the lab setup.

In a given measurement the modulation factor for a completely polarized beam μ_{100} can be used in conjunction with the modulation factor of the beam being measured, to find the unknown polarization P,

$$P = \frac{\mu_p}{\mu_{100}} \tag{6}$$

To determine the minimum detectable polarization (MDP) of a specific detector design we use,

$$MDP(\%) = \frac{n_\sigma}{\mu_{100} R_{src}} \sqrt{\frac{2\left(R_{src} + R_{bgd}\right)}{T}} \tag{7}$$

where n_σ is the significance level (number of sigma), R_{src} is the total source counting rate, R_{bgd} is the total background counting rate and T is the observation time. In terms of detector development, increasing the modulation factor for 100% polarized measurement μ_{100} or the source count rate R_{src} (increasing the effective area of the detector), will decrease the MDP of the detector.

CHAPTER III

THE GRAPE CONCEPT

Initial Concept

The design of a Compton polarimeter is based on several criteria. The ability of the detector to reconstruct the kinematics of single scattering events, while eliminating multiple scattering events, is of ultimate importance. As mentioned earlier, GRAPE utilizes a design that incorporates two detector types; an array of scattering detectors surrounding a central calorimeter detector. In event reconstruction the measured parameters include the location of the Compton interaction, the energy of the scattered electron and the energy/direction of the scattered photon. The scattering detectors provide us with the Compton scatter location of the incident photon and the energy of the recoil electron. The scattered photon is then detected by the calorimeter, where its energy deposit and interaction location recorded. The ability of the detector to determine the modulation pattern, and hence the polarization parameters, is directly influenced by the accuracy with which we can determine this kinematic information.

Principles of Operation

The development and design of the GRAPE detector has evolved through three laboratory science models [2-10]. Each one represented a successive improvement, but all three essentially operated under the same underlying principle of operation. A high-Z

material, the calorimeter, is surrounded by multiple plastic scintillation detectors that serve as a target for the Compton scattering. The entire array is contained within a single light-tight housing. The plastic scintillators are made of a low-Z material that maximizes the probability of a Compton interaction. The purpose of the calorimeter is to fully absorb the energy of the scattered photon. Ideally, photons that are incident on the plastic scintillator array will Compton scatter only once, and then be subsequently absorbed by the calorimeter. For such an event we measure the energy of the scattered electron in the plastic and the deposited energy of the scattered photon in the calorimeter. With multiple plastic scintillators surrounding the calorimeter, we can determine the azimuthal scatter angle of each valid event. A histogram of the azimuthal scatter angle provides a measurement of the polarization parameters (magnitude of the polarization and polarization angle) of the incident flux.

In order to accurately measure the azimuthal modulation (and hence the polarization parameters), we need to correct for geometric effects specific to the individual detector design. When the azimuthal modulation profile is generated, the distribution not only includes the intrinsic modulation pattern due to the Compton scattering process, but it also includes various geometric effects. One of these effects originates from the specific layout of the detector elements within the polarimeter and the associated quantization of possible scatter angles. Other effects include such things as the nonuniform detection efficiency of the PMT used for detector readout. In order to correctly analyze the data we first measure unpolarized radiation with the polarimeter. These data provide a measure of the various geometric effects. By dividing the polarized distribution by the unpolarized distribution and then normalizing with the average of the

unpolarized distribution we obtain a corrected distribution with the geometric effects eliminated (Fig. 7.) In the laboratory, these effects are easy to measure using data from an unpolarized beam. In practice, simulations may be used to determine the unpolarized modulation pattern that is used to correct the measured data.

GRAPE History

Science Model 1 (PSPMT Design)

Science Model 1 (SM1) was designed so that the entire device fit on the front end of a 5-inch diameter position-sensitive PMT (PSPMT) (Hamamatsu R3292) [2-4]. The scattering detector array consisted of 250 plastic scintillators, Bicron BC-404, each 5mm × 5mm × 50mm. Each was wrapped in Tyvek® in order to maximize the light collecting ability of each plastic and to eliminate cross talk between elements. Kapton® tape was used to secure the Tyvek® wrap on each plastic. The array of plastic elements was arranged, Fig. 6, with a square void in the center allowing for the insertion of the calorimeter. The calorimeter was a 2 × 2 array of 1cm × 1cm × 5cm CsI(Na) elements coupled to a 2 × 2 multi-anode PMT (MAPMT) (Hamamatsu R5900). The calorimeter detector was enclosed in its own light-tight housing and placed within the central void of the plastic array.

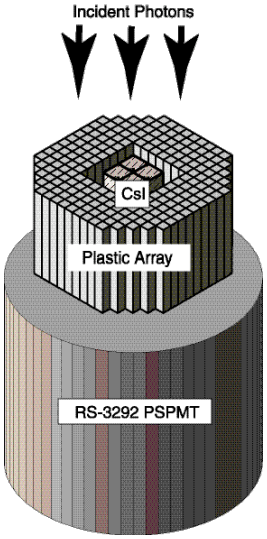

Figure 5: The SM1 design concept.

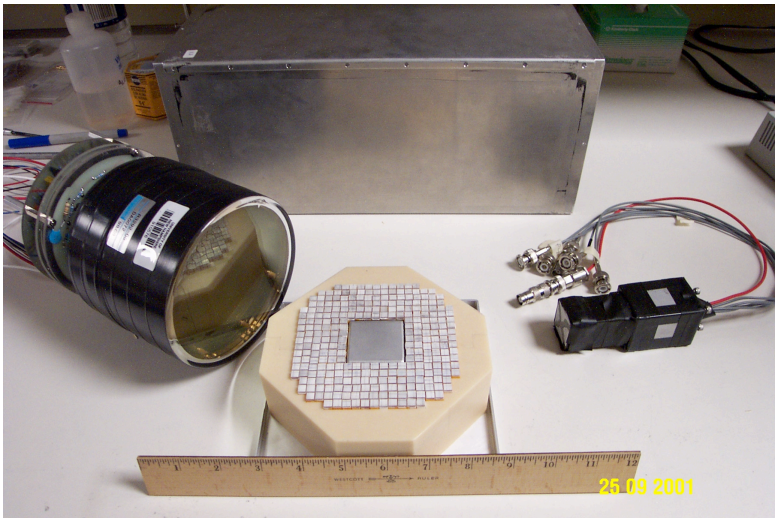

Figure 6: The SM1 detector with the PSPMT (left), the plastic scintillator array (middle), and the calorimeter assembly (right).

The PSPMT made use of a charge division network for readout that provides a weighted average of the spatial distribution of the measured light output using only four signals (two in x and two in the y). The MAPMT also has four outputs, one for each of

the anodes coupled to a single CsI(Na) crystal. Valid events were recorded for a signal in the PSPMT and a signal in one CsI(Na). This method does not allow us to distinguish multiple scatters in the plastic array. The signal from the PSPMT only contains the weighted average of all light signals generated in the plastic scintillator array.

The level of polarization measured by SM1 was 55(±2)%, in agreement with the expected value of 55-60% [2-4]. These results verified both the operation of the SM1 prototype and the efficacy our computer modeling.

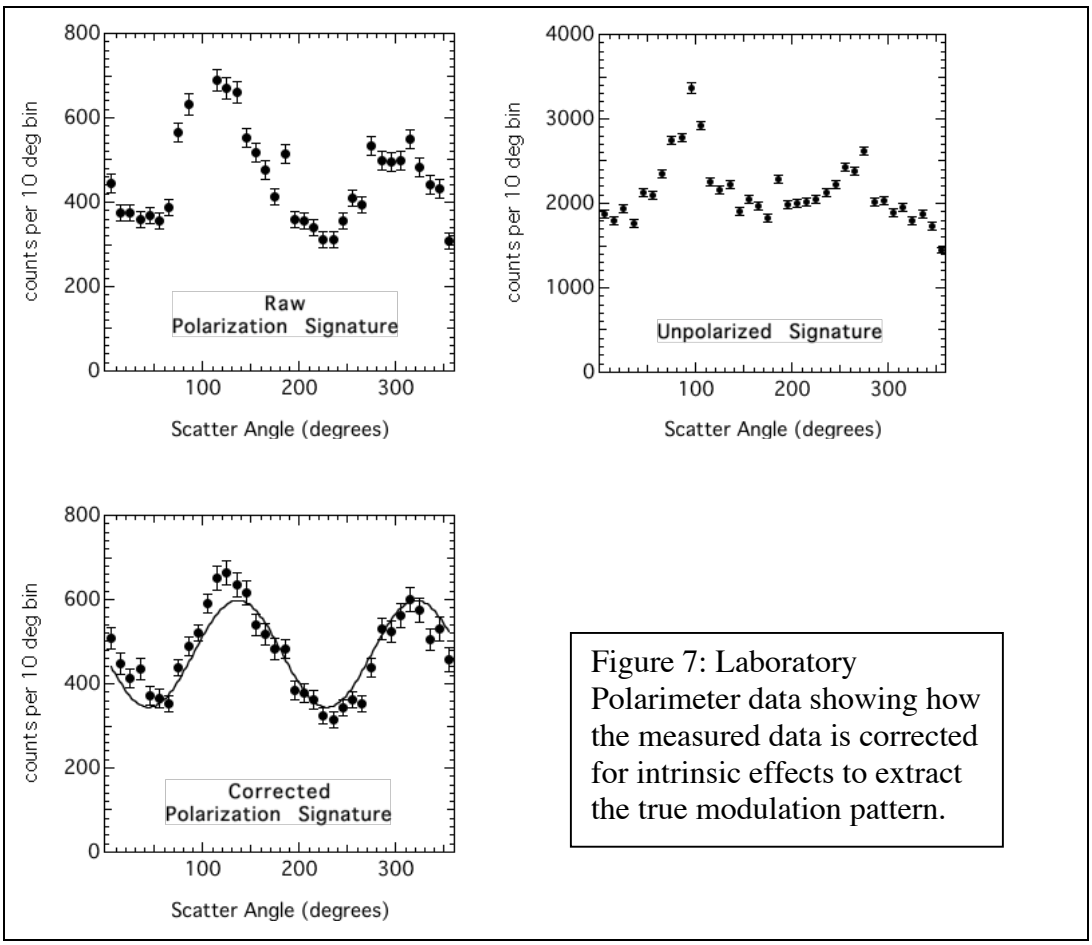

Figure 7: Laboratory Polarimeter data showing how the measured data is corrected for intrinsic effects to extract the true modulation pattern.

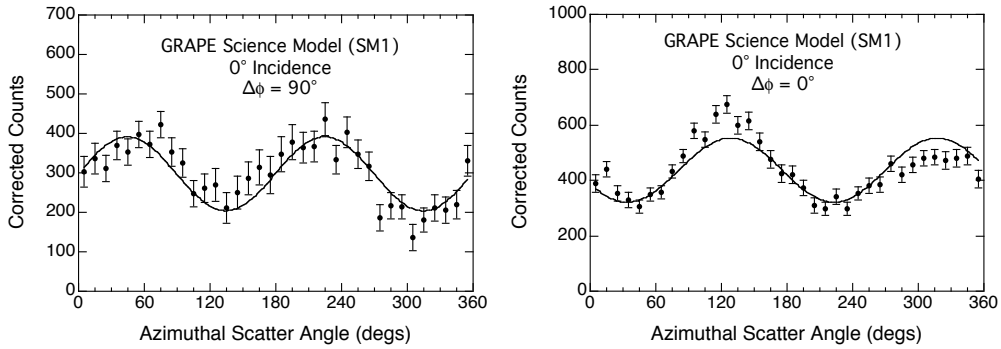

Figure 8: Results from SM1 showing the 90° shift in the modulation pattern.

An Improved Design

MAPMT Design

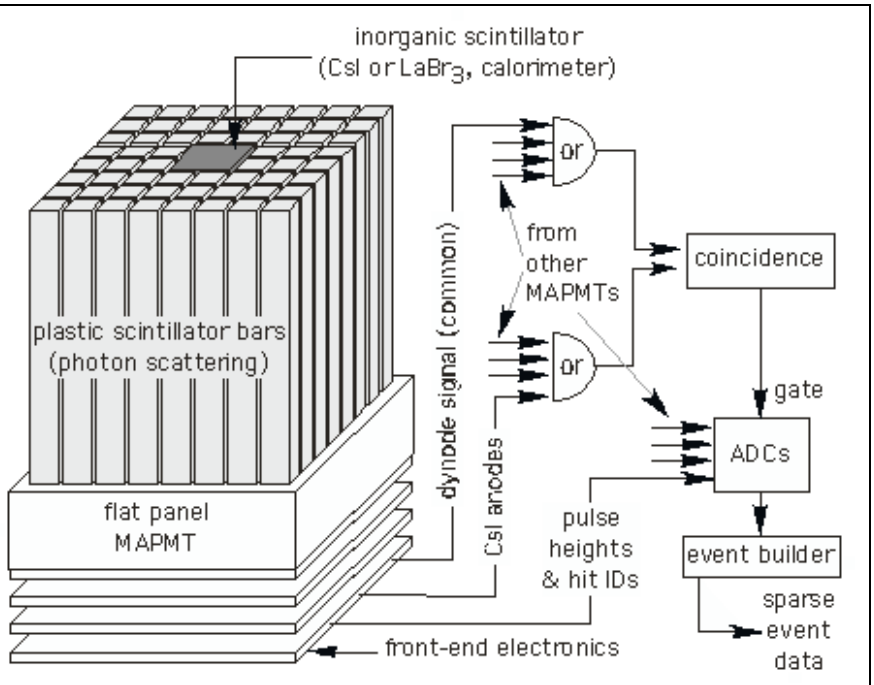

Figure 9: The MAPMT design concept with 60 plastics surrounding a central CsI(Na) crystal.

Following on the success of SM1 we developed a more compact design based on the use of a flat-panel multi-anode photomultiplier tube, (Hamamatsu H8500) [6-10]. The H8500 is a MAPMT with an array of 8 × 8 independent anodes. The 5 mm anodes are arranged with a pitch of 6 mm, occupying a total sensitive area of 52 mm × 52 mm. With a depth of 28 mm, the flat-panel PMT is far more compact than the PSPMT used in SM1.

Figure 10: The Hamamatsu H8500 MAPMT (top), and several plastic scintillator elements (bottom).

The MAPMT design offers several advantages over the SM1 design. One advantage is that the entire polarimeter can be contained in a single housing with one readout device. There is no need to use a second PMT for the calorimeter; the complete array is coupled directly to the face of the H8500, which is used to readout both plastics

and calorimeter. This eliminates the need for second HV line and reduces the overall mass of the polarimeter. More importantly it eliminates the obstructive mass of the MAPMT used for the readout of the calorimeter array in the SM1 design. The square design of the MAPMT also allows for the close packing of multiple modules with minimal dead space. Compared to a single SM1 module, an array of four MAPMT modules provides approximately 60% larger effective area and a 30% smaller footprint. The much smaller depth of the MAPMT design also results in a smaller volume.

Science Model 2 (SM2)

In order to move forward into testing the MAPMT design we began with science model 2 (SM2). SM2 was a result of the fact that we lacked the electronics needed to process all the available channels of the MAPMT. Although it did not fully utilize the capabilities of the MAPMT, it allowed us to move forward with the development program.

The SM2 design utilized an array of 12 plastic scintillators measuring 1 cm × 1cm × 5 cm, all wrapped in Tyvek® and Kapton® tape. Each plastic scintillator was read out with a group of four MAPMT anodes. The signals from within each group of four anodes were summed together, providing a total of 12 data channels for the scattering elements, Fig. 11. The center four anodes were used to read out the CsI(Na) calorimeter, a single crystal 1 cm × 1cm × 5 cm. The whole array assembly was held together with cookie spacers made from Delrin® and coupled to the face of the MAPMT with optical grease. This setup allowed for initial measurements with the new MAPMT design to evaluate

some of the fundamental characteristics of the design without significant changes to the data acquisition setup. Laboratory results from SM2 are discussed in chapter four.

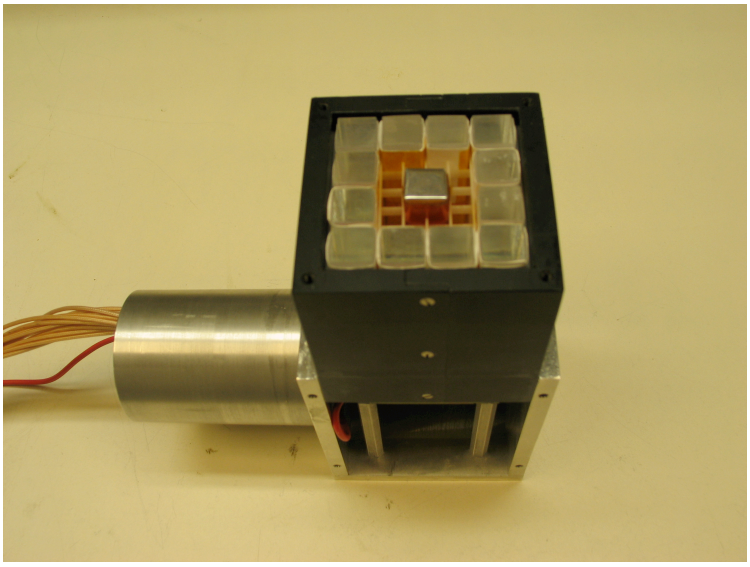

Figure 11: SM2 in initial testing phase with large plastics populating four anodes for a total of 12 scattering elements.

Science Model 3 (SM3)

With the first tests of SM2 completed successfully, the MAPMT was fully populated with 60 plastic scintillators, (each 5mm × 5mm × 5cm in size), according to the original MAPMT design (Fig. 9). As with SM2, the plastic scintillators are wrapped in Tyvek® and Kapton® tape. In order to ensure proper spacing of the elements on the MAPMT anodes, cookies made of Delrin® were fabricated to hold the array together as one complete piece, Fig. 12. The whole array is coupled to the MAPMT using clear G&E silicon. This was done after testing revealed a significant number of air bubbles present

when optical grease was used. Using the silicon greatly reduced the number of air bubbles and in turn increased the light output measured in the MAPMT anodes. The silicon also offers the advantage of being more secure, making the handling of the detector easier in the lab. The whole detector is housed within a light tight aluminum and Delrin® case seen in Fig. 11.

A small piece of lead, 1cm × 1cm × 5mm, was placed over the CsI(Na) calorimeter to shield it from incident photons. According to the polarimeter design, we want incident photons to initially scatter in the plastic array not in the CsI(Na). By attenuating photons incident to the CsI(Na) detector we can eliminate the number of false events recorded. These false events are essentially background and by equation 7, if we reduce the background counting rate we reduce the minimum detectable polarization of the polarimeter (increases sensitivity.) Laboratory results from SM3 are discussed in chapter five.

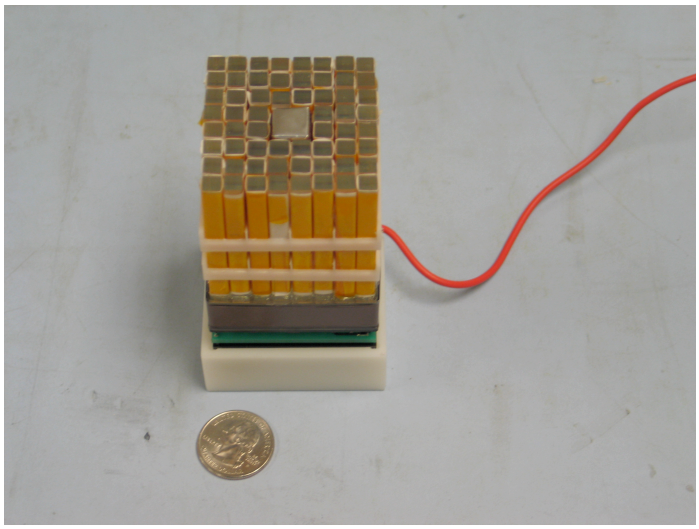

Figure 12: SM3 fully populated with 60 plastics and central CsI(Na) calorimeter.

CHAPTER IV

SCIENCE MODEL 2 RESULTS

Experiment Setup

For each of the three science models, measurements were conducted in the laboratory to characterize the response of the detector. In order to properly characterize the polarimeter response, a source of polarized photons was required. The polarized radiation used in the tests was produced by Compton scattering radiation from a laboratory gamma-ray source [2, 42]. Radiation from a ^{137}Cs source is collimated with lead shielding and directed toward a plastic scintillation detector, referred to as the polarizer. Photons with an initial energy of 662 keV scatter through an angle of 90° before reaching the polarimeter. The scattered radiation reaching the polarimeter is highly polarized (at a level of ~55-60%) and has a reduced energy of 288 keV. The use of the active polarizer also allows us to electronically tag the Compton scattered (polarized) photons. A triple coincidence between the polarizer and the two sets of polarimeter detectors provides an efficient means for recording data from the polarized beam.

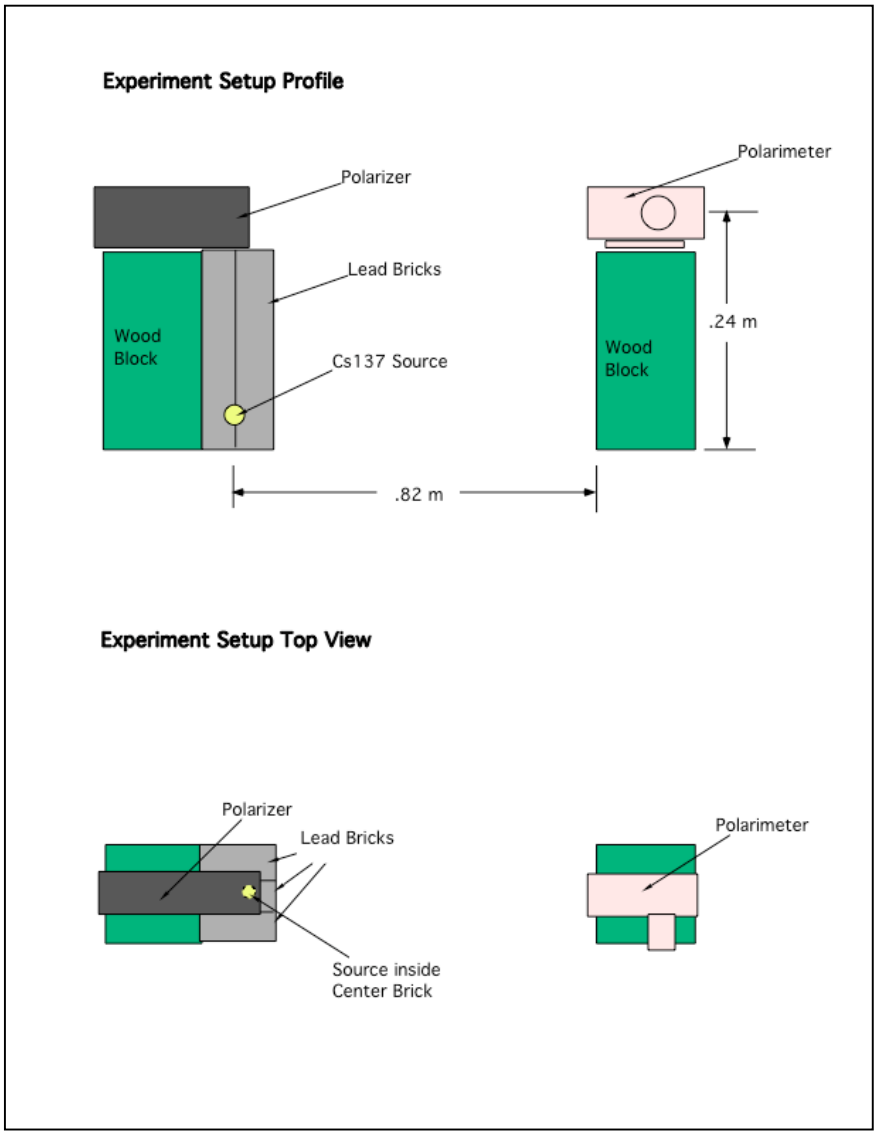

Figure 13: Experimental setup for GRAPE polarized measurements.

SM2 Data Acquisition

The SM2 data acquisition system utilized a combination of NIM and CAMAC modules to perform the signal processing. A block diagram for the SM2 data acquisition

set up is seen in Fig. 14. The large plastic elements of SM2 each covered four independent anodes of the MAPMT. These four channels were grouped together to output one anode signal for each of the 12 plastic elements. The CsI calorimeter also covered four anodes and was summed in the same way producing a single output channel. These 13 output anode channels were connected directly to a CAEN N568 spectroscopy amplifier for signal processing. The spectroscopy amplifier split the input anode signals into slow and fast outputs. The fast outputs are used for timing purposes and the slow outputs are used for pulse height analysis.

The fast signals from each plastic element were sent to one of two LeCroy integral discriminators (Models 821 & 4608C). The model 821 is a four channel integral discriminator. The 4608C is an eight channel integral discriminator. Together these two modules provided an independent discriminator for each plastic element. Integral discriminators work by generating a logic signal when the input pulse height exceeds a programmed level. The discrimination levels for each channel were independently set in order to eliminate low energy background. When the input pulse to the discriminator exceeded the programmed threshold limit a logic pulse was sent to a LeCroy Logic unit (Model 429A). The Logic unit was set in an OR mode which in turn produced a logic pulse if any one of the plastic elements had a signal above threshold.

The fast signals from the polarizer and CsI(Na) calorimeter were processed in a similar fashion with the exception that constant-fraction-discriminators (CFDs) were used in the threshold determination. The logic pulses from the polarizer, calorimeter, and the plastic logic unit were sent to a gate generator Philips Scientific Model 794, producing gates for coincidence evaluation in the LeCroy (Model 365AL) Logic unit. The logic unit

was used to produce gates corresponding to a programmable coincidence level. This gate is then sent to the ADCs to activate the pulse height conversion.

Each slow signal from the spectroscopy amp was sent to one of two ADC's (Ortec AD811) housed in a CAMAC crate. Controlling the functions of the CAMAC crate is a SCM301 crate controller. The ADC's performed pulse height conversion of the anode signals during an active gate sent to them from the logic circuit located in the NIM crate. Logic gates are generated when the appropriate coincidence for the detectors is valid (i.e. triple coincidence for polarized data).

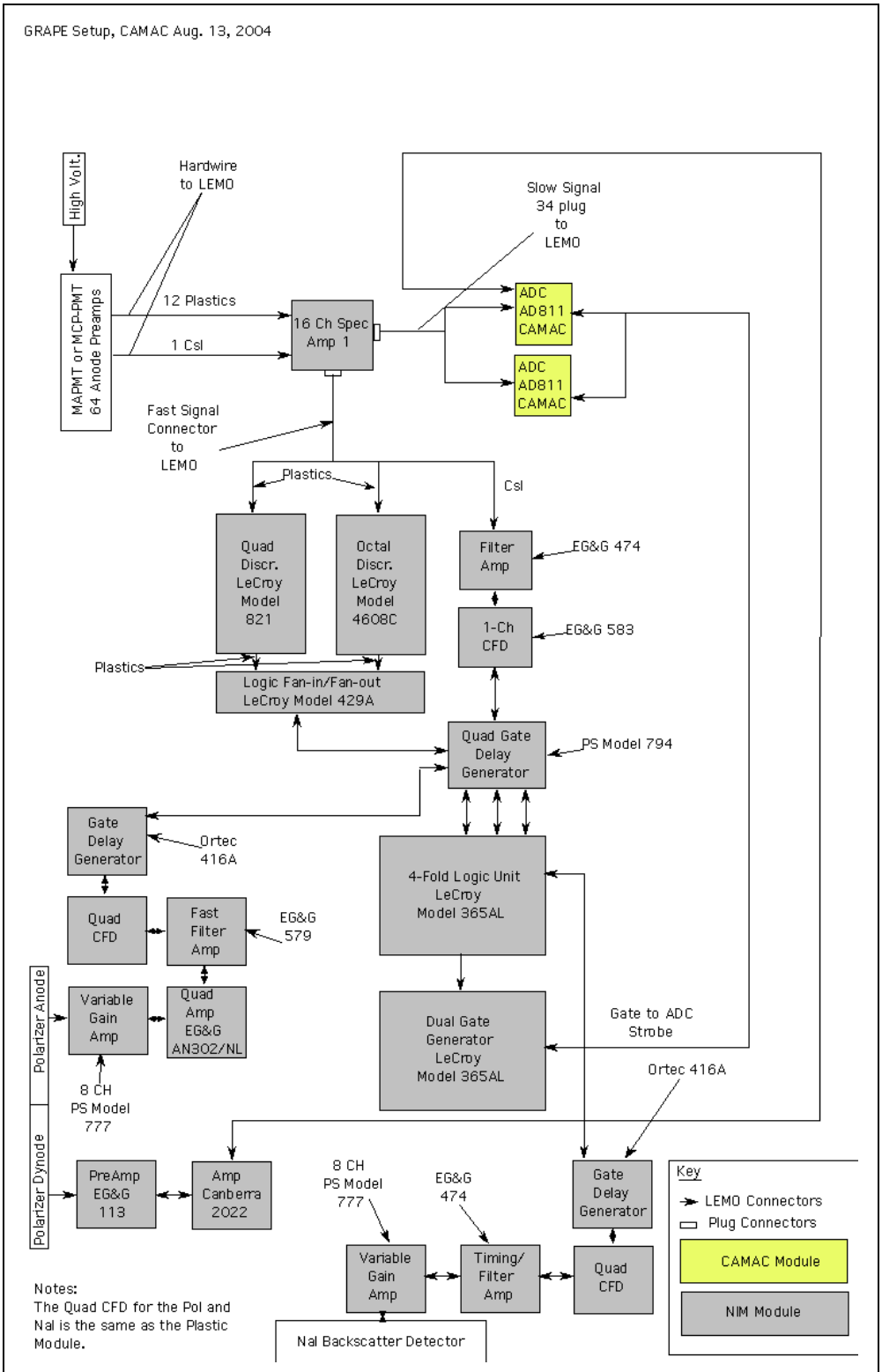

Figure 14: Block diagram for the SM2 electronics.

SM2 Software

The data acquisition software acts as a link between CAMAC/VME electronics and the desktop computer. Data that is generated in ADCs needs to be transported from their output buffers to files on the desktop for subsequent analysis. Our setup uses a Macintosh G4 computer running MacOSX (v10.3). Software purchased from Sparrow Corp., KMAX v7, is used to control the CAMAC crate through the SCM301. The SCM301 controller in the CAMAC crate is linked to the Macintosh computer through a serial cable. The two ADCs in the CAMAC crate perform pulse height conversions when triggered by logic gates. The ADCs have no internal output buffer so data must read from them before subsequent conversions take place. The KMAX software is programmed to poll the ADCs and look for a data ready flag. When the flag is present, the SCM301 reads the converted values on the ADC channels and sends the data to the computer. The SCM301 then clears the data from the ADCs, readying them for the next event.

The data read from the ADCs is histogrammed on the KMAX desktop for real time viewing of the data being read. KMAX also stores the data into an output text file to be used in subsequent data analysis.

Data Processing

The data written in the GRAPE event files is analyzed using the ROOT software package (from CERN). ROOT performs data processing (incorporating energy calibrations, filtering out invalid events, etc.), event selection and analysis. It is with ROOT that we apply the energy calibration to each detector. We can then look at each event and determine its validity. As stated earlier, we are interested in events occurring in

a single plastic element in coincidence with events in the calorimeter and the polarizer. By analyzing the recorded energies in all the plastics for each event we can determine whether single or multiple Compton scatters occurred. Once a valid event is identified the scattering angle is recorded and histogrammed.

Energy Calibrations

Energy calibrations were conducted in the laboratory using several radioactive sources. Calibrations needed to be done for all the individual plastics elements, the CsI(Na) calorimeter and the polarizer. There were two methods employed to accomplish these calibrations, direct and backscatter measurements. Placing a calibration source directly incident to the detector being calibrated produces either a photo peak (complete absorption) or Compton edge depending on the type of detector and the photon energy. For the plastic detectors (the plastic array in the polarimeter and the polarizer), photopeak calibration is only possible using the low energy source, ^{241}Am (~60 keV). Higher energy sources will produce a Compton edge in plastic scintillator detectors. This is due to their low-Z composition creating a high probability of Compton scattering in these elements (the reason why we use them as scattering detectors.) A Compton edge is the upper limit on absorbed energy from a single Compton scattered photon and corresponds to a 180° scatter. The calorimeter, a high-Z material, has a higher probability of complete photon absorption, which results in photo peaks for all calibration sources.

In theory, a Compton edge should be a clear edge, but due to the possibility of multiple scatters higher energies can be recorded. This results in a sloping edge making in difficult to accurately determine the precise location of the Compton edge. Backscatter

techniques were used in order to more accurately calibrate the plastic detectors. By using a second detector, we use a NaI detector; we can utilize the logic portion of our setup and record only events that scatter ~180° in the detector being calibrated and are subsequently absorbed by the NaI detector. This will create a double coincidence in our logic and a gate will be sent to the ADCs initiating the read of the energy deposited in the detector being calibrated. The recorded spectrum of the detector being calibrated will result in a peak that is centered on the energy deposited in the detector for ~180° backscatters. This peak is located at the same energy as the Compton edge, but with a more defined location. This technique allows us to more accurately calibrate plastic detectors for higher energies.

SM2 Calibrations

Calibrations of SM2 were performed in the spring of 2004. The polarizer and CsI(Na) calorimeter were calibrated individually while the plastic elements were calibrated as a group. Each plastic detector element has its own energy calibration. The polarizer was calibrated using the backscatter technique (Fig. 15) with ^{137}Cs and ^{133}Ba laboratory sources and direct with ^{241}Am. Another point used for the calibration was the pedestal value (zero energy) of the detector. This is accomplished by sending the ADCs a false gate for a detector with no source present. It results in a sharp peak, which represents the channel in the ADC corresponding to no measurement for a detector (~0 keV.)

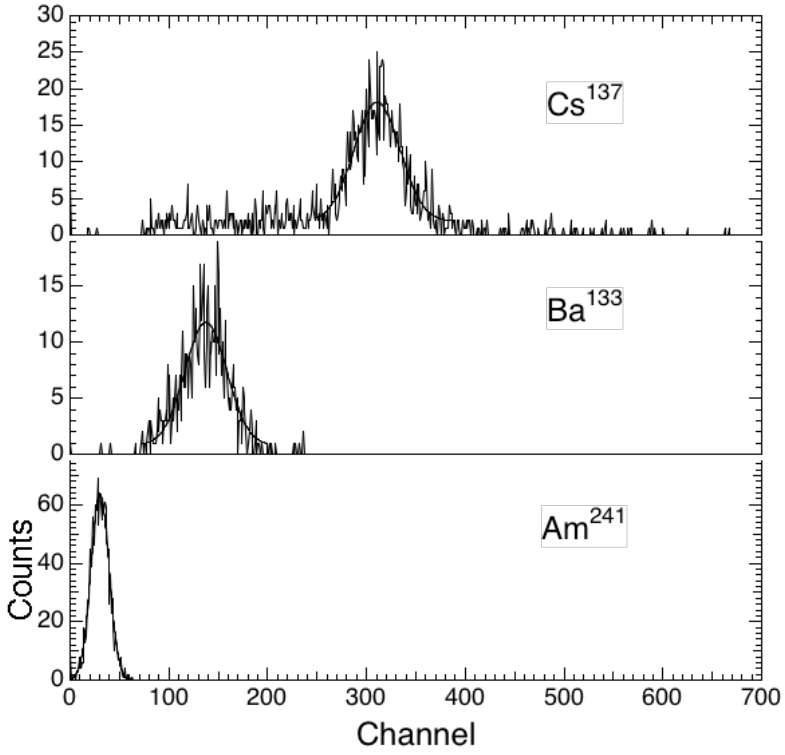

Figure 15: SM2 polarizer calibrations spectra. Backscatter techniques were used for the ^{137}Cs and ^{133}Ba sources while the ^{241}Am was measured directly.

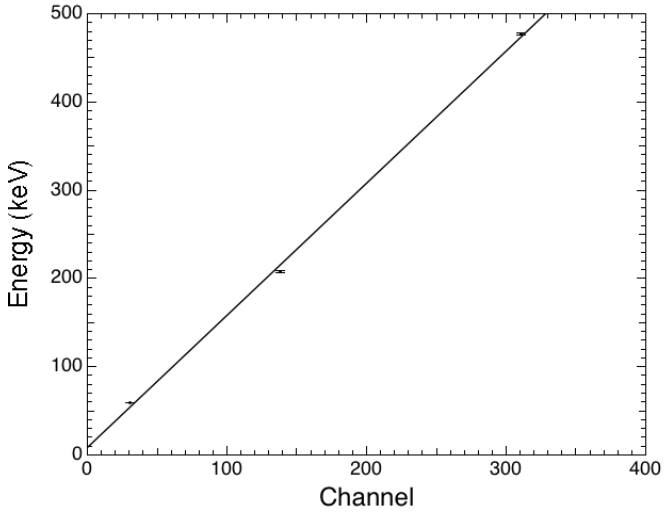

Figure 16: Energy vs. Channel plot used to determine polarizer energy calibration.

Four laboratory sources were used (Fig. 17) to calibrate the calorimeter measured directly; ^{137}Cs , ^{133}Ba, ^{57}Co, and ^{241}Am.

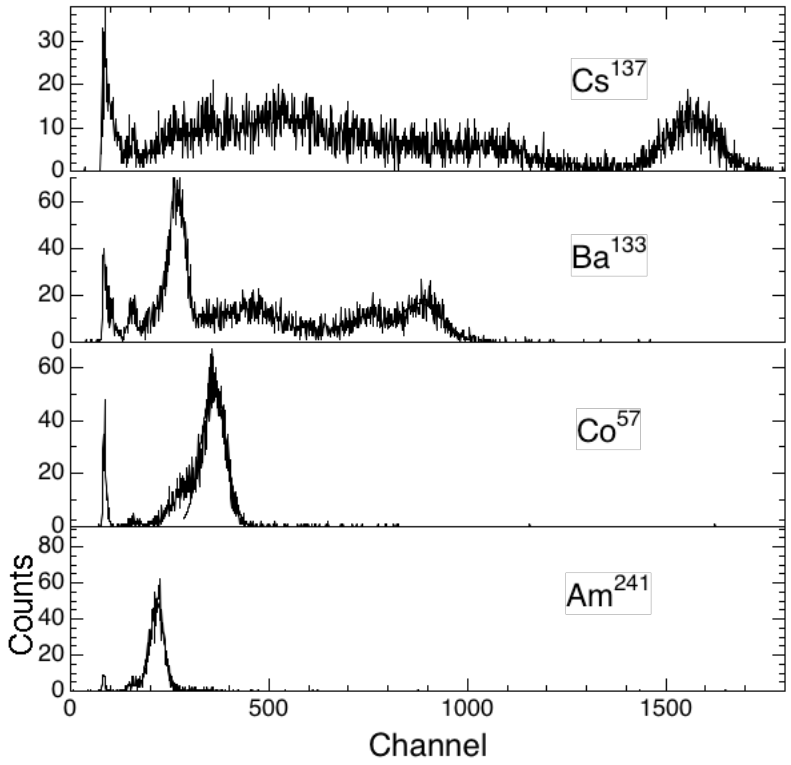

Figure 17: SM2 CsI calibration spectra. All four sources are measured directly.

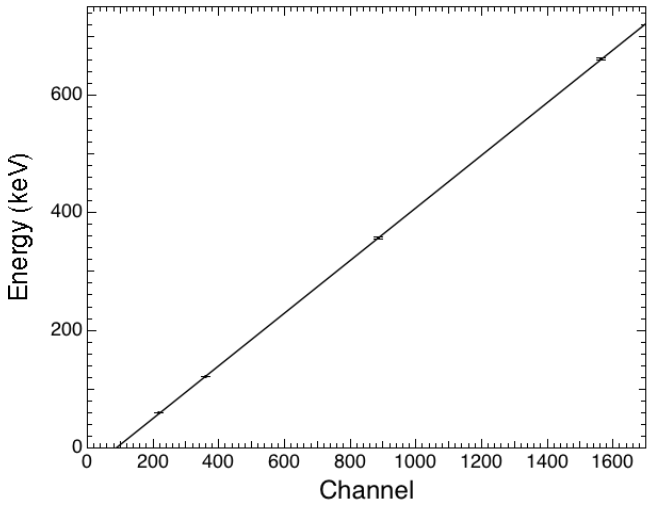

Figure 18: Energy vs. Channel plot used to determine CsI energy calibration.

The plastics were calibrated as a group using three sources: ^{137}Cs , ^{133}Ba, ^{241}Am (Fig. 19.) The Compton edge values were used for the ^{137}Cs and^{133}Ba, while it was possible to obtain a photo peak for the lower energy ^{241}Am.

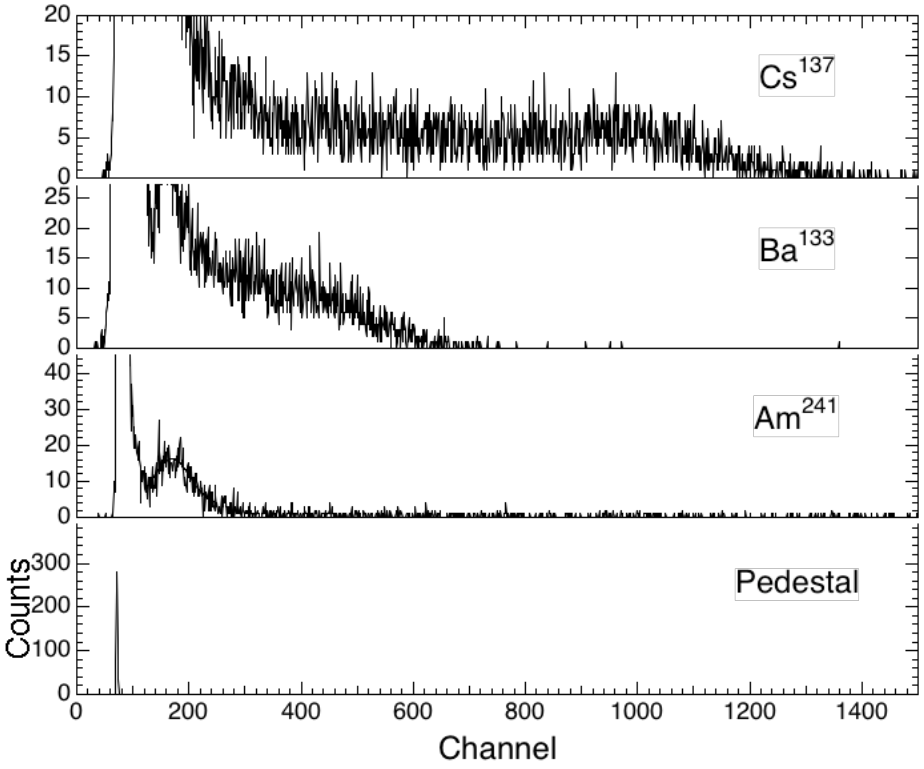

Figure 19: SM2 plastic calibration spectra. All three sources are measured directly. This plot represents the calibration for a single plastic.

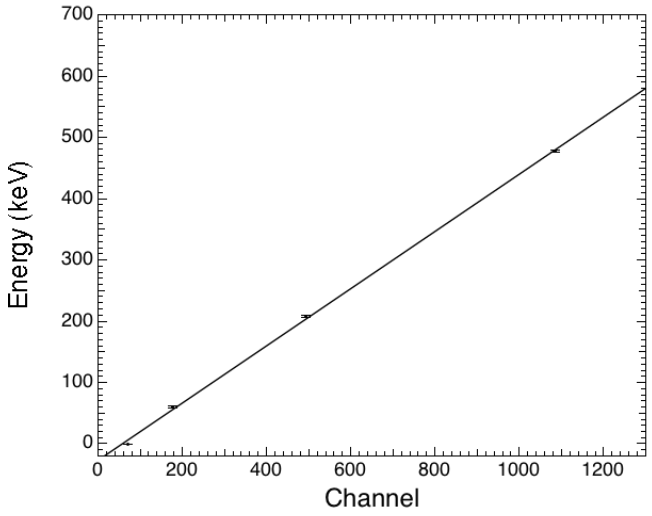

Figure 20: Energy vs. Channel plot used to determine plastic energy calibration.

SM2 Results

Laboratory tests of SM2 were conducted during the summer of 2004 with polarized radiation at two different polarization angles, 0° and 90°. Each test measured incident polarization for ~6 days. The polarized radiation was created in the lab according to the experimental setup and the data were corrected as described in the principles of operation. For these measurements the polarized beam was vertically incident on the front surface of the polarimeter. The corrected plots for the two polarization angles are shown in Fig. 21.

For the data collected at 0° polarization angle, a fit with Equation 3 yielded a modulation factor of 0.28(±)0.06, corresponding to a measured polarization level of 55(±14)%, in agreement with the 55-60% value expected. For the data collected at a 90° polarization angle, the measured polarization level was 53(±9)%, again consistent with the expected value. Simulations done with MGEANT predicted μ_{100} for this detector

configuration to be 0.48(±)0.03, which was used to derive these polarization levels (following equations 3, 4, and 5.)

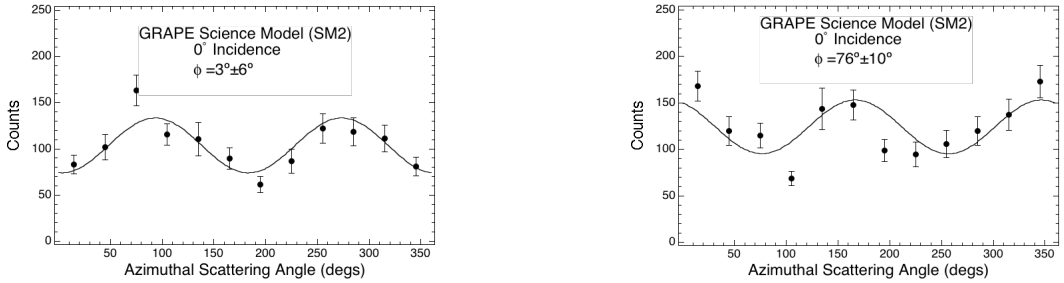

Figure 21: Results from SM2 showing the 90° shift in the modulation pattern when rotating the detector 90° to the incident polarization vector.

CHAPTER V

SCIENCE MODEL 3 RESULTS

Hardware

Along with the changes in detector design from SM2 to SM3 we also modified the data acquisition system to handle the increased number of data channels. The total number of data channels increased from 14 (in SM2) to 62 (in SM3), (including the plastic scattering elements, the polarimeter, the polarizer). Another change in the hardware was the use of VME electronics for the data acquisition in SM3. In SM2 a CAMAC crate along with NIM electronics was used. NIM electronics are also used in the data acquisition system of SM3.

SM3 Hardware

The SM3 data acquisition setup utilized a combination of NIM and VME modules, Fig. 23. Preamp boards were designed to be attached to the output pin assembly on the base of the MAPMT, Fig. 22. Each preamp board handles 16 anode channels plus 1 test channel. The function of the preamps is to terminate the capacitance quickly in order to maximize the signal-to-noise ratio. Four boards are required to handle all 64 channels. These boards are small enough to fit within the footprint of the MAPMT (Fig. 9). All signals are processed in CAEN spectroscopy amplifiers (MOD. N568), which splits each signal into fast and slow outputs.

Each slow signal from the MAPMT is sent to the ADCs located in a VME crate for the pulse height conversion. Also housed in the VME crate is a CAEN constant fraction discriminator (CFD, CAEN V812) with 16-channel capability. Constant fraction discriminators are used in the plastic array to improve the timing capabilities of the SM3 data acquisition system. A CFD functions differently from a regular discriminator. The

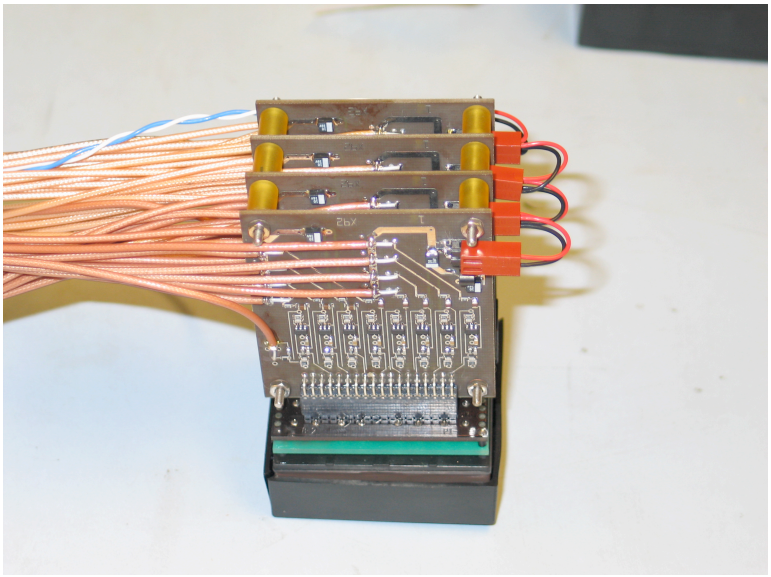

Figure 22: The preamp circuit boards plugged into the back end of the MAPMT.

discriminators used in the SM2 plastic array would produce a logic signal when the input exceeded the programmed threshold regardless of the pulse height above that threshold. This can result in slight differences in timing characteristics due to the fact that a larger pulse will reach the threshold before a smaller pulse even if both are over threshold. This is because the pulses all have the same rise time regardless of their pulse height. A CFD will invert incoming signals and sum them to produce a bipolar signal that always crosses

the zero point at the same time regardless of pulse height. This now allows for identical timing despite the differences in pulse height.

In order to use the single CFD module to monitor the 60 fast signals from the plastic scintillators, a passive sum box was designed and built to combine the signals from the plastic scintillators into 15 groups. The gain-matched fast signals from each group were sent to the sum box and the single sum output sent to the CFD. The CFD has an OR output option, which functions by outputting a logic signal when at least one of its 16-channels is above the programmed threshold. This works because we are interested in single events occurring in any one plastic. When a signal above the CFD threshold occurs in any one plastic group, a logic signal is sent to the logic portion of the setup for coincidence determination. Although this limits our ability to identify multiple Compton scatters in the plastics (it is possible that up to four could happen within each group).

The VME-based CFD only monitors the fast plastic signals. Separate NIM-based CFDs are used for the polarizer and calorimeter channel. The NIM-based CFDs are adjusted individually for threshold and delays. Each CFD will then send a logic signal to the coincidence portion of the setup when programmable threshold levels are exceeded for each detector.

The coincidence (logic) piece of the setup consists of 1) a PLS 794 Quad gate generator 2) a LeCroy 365AL 4-Fold Logic Unit 3) a LeCroy 222 Dual gate generator. The three logic signals (plastic, CsI(Na), polarizer) are input to the PLS 794 in order to create gates for each channel. The gate widths are set according to the speed of each detector, the CsI(Na) ~100ns, having a much slower rise time compared to the plastics ~20ns. These gates are fed to the logic unit where an AND circuit allows the user to

select the level of coincidence. For example, a polarized run would be set to have the three gates active, requiring a triple coincidence level. When energy calibrations are needed using a laboratory gamma-ray source, the appropriate detector can be selected and the level of coincidence set to single. The output of the logic unit is sent to the LeCroy gate generator, which generates a gate that is used to trigger ADC conversion.

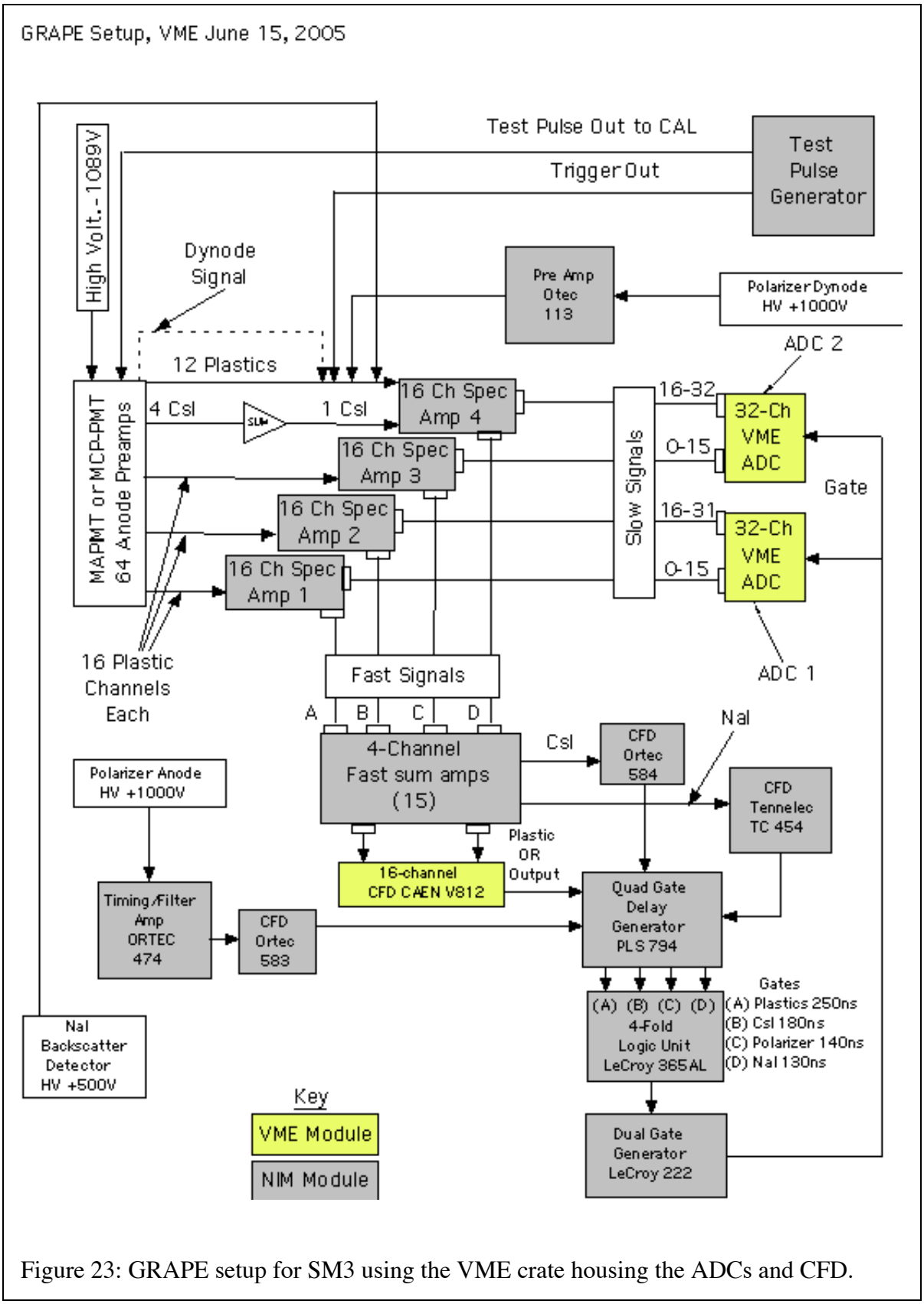

Figure 23: GRAPE setup for SM3 using the VME crate housing the ADCs and CFD.

SM3 Software

The CAEN M785 ADCs each have the capability to store 32 events (32 pulse height conversions), in their output buffer. The two ADCs used give us a total of 64 available channels. Controlling the operation of the VME crate, the two ADC VME modules and the CFD VME module is achieved using KMAX version 8.03. KMAX allows control of the VME crate through the SBS 620 controller VME card and PCI board. KMAX communicates to VME modules through a fiber optic cable connected from the SBS PCI card in the Mac to the SBS controller module housed in the VME crate.

The ADC's must be properly programmed before they can function properly. The proper sequence is: 1) reset ADC; 2) activate all channels; 3) disable zero suppression to ensure the readout of all channels regardless of conversion value; 4) setting of all channel thresholds to zero. Disabling zero suppression allows the ADC to report all 32 channels of data. All channel thresholds are set to zero because we need all channel data during an event. The majority of the programming effort lies with acquiring the data from the output buffers of the ADC.

Due to the fact that we are using two ADC's to acquire data, synchronization becomes a very important factor. When the ADC's 32 event output buffer is full, a flag is written at a specific address. KMAX continuously polls this address and waits for the flag to be set. When it sees that the flag has been set, KMAX initiates the acquisition portion of the program. The ADC's are shut off and all events are read from the buffers. The ADC's tag all data with an event number and it is this number that is used to determine the synchronization. If the ADC's are off in event numbers the event block is deleted as

unusable data. This can happen when the ADC's are turned on. If the event rate is high enough or just a random coincidence happens, the first ADC can receive a gate before the second one is turned on. This requires that all data be checked for synchronization prior to writing to the data file. After the data is read the ADC's are again turned on to begin acquiring data. During our polarization experimental runs this problem has not been evident with event rates typically ~.4Hz, but during energy calibrations it can be a problem if event rates are too high (>45Hz.)

Other programming involved with Kmax is the initialization and setup of the VME CFD. Similar to the ADC's the CFD must be reset and all channels activated. Each channel is programmed with a threshold value specific to its gain. When there is a valid event occurring in any plastic group the fast signal exceeds the programmed threshold and a logic signal is sent to the gate generator.

SM3 Calibrations

Calibrations for SM3 were performed in the spring of 2005. Again the polarizer, calorimeter and plastic detector elements were each calibrated separately with the plastic detector elements done as a group, each plastic having its own calibration. For the polarizer, backscatter techniques were used with ^{137}Cs and ^{133}Ba and a direct measurement of ^{241}Am providing a third source (Fig. 24.)

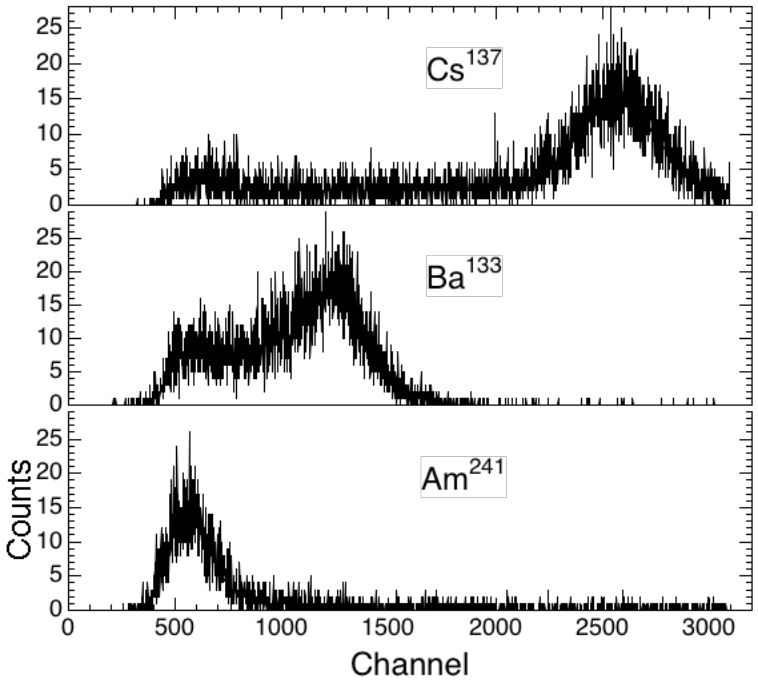

Figure 24: SM3 polarizer calibrations spectra. Backscatter techniques were used for the ^{137}Cs and ^{133}Ba sources while the ^{241}Am was measured directly.

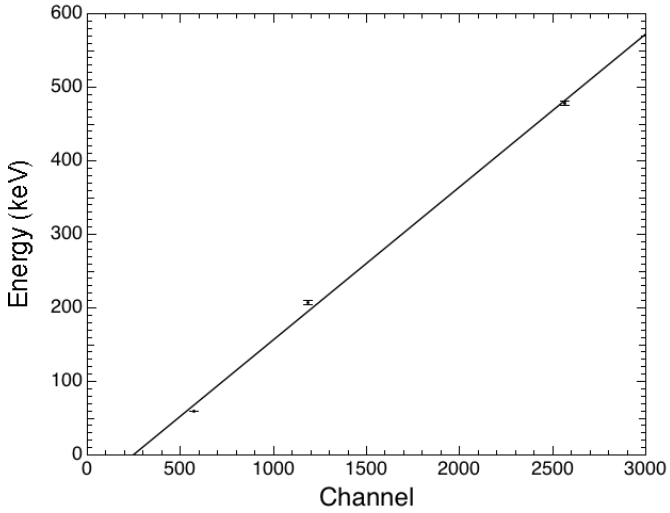

Figure 25: Energy vs. Channel plot used to determine polarizer energy calibration.

The CsI(Na) calorimeter was calibrated using direct sources, ^{137}Cs , ^{133}Ba, and ^{241}Am (Fig. 26.)

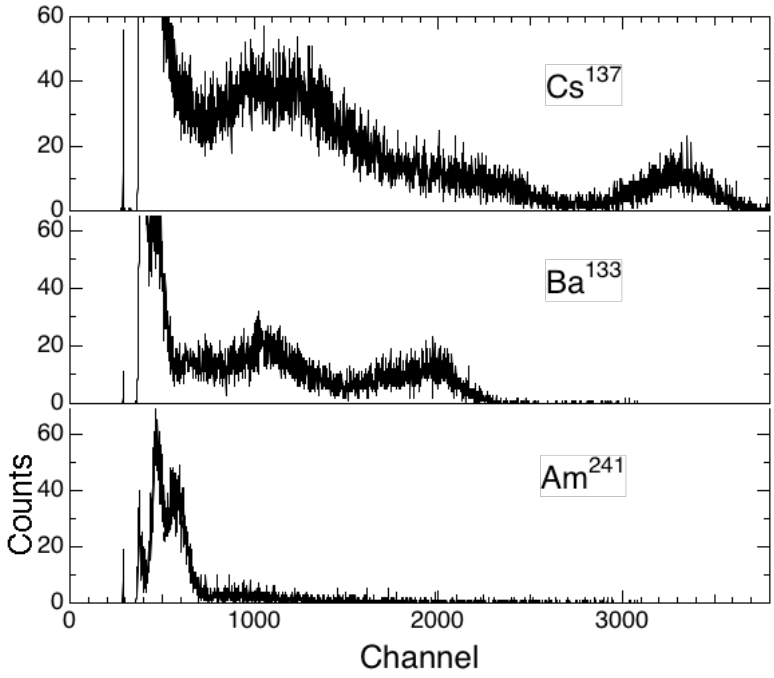

Figure 26: SM2 CsI calibration spectra. All four sources are measured directly.

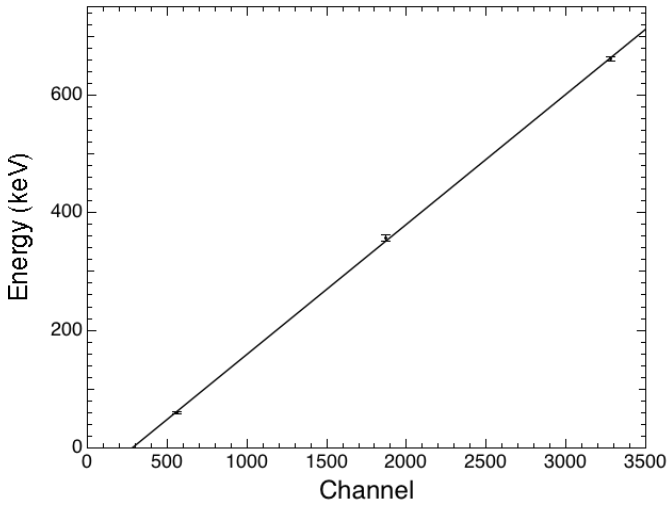

Figure 27: Energy vs. Channel plot used to determine CsI energy calibration.

The plastic element calibrations were performed with the backscatter technique for ^{133}Ba and ^{57}Co, (Fig. 29 and Fig. 30.) The pedestal for each plastic was used for a third measurement. Due to the geometry of the SM3 plastic array, ~5cm square, consideration was taken to ensure that the backscatter technique was valid. As can be seen in the setup for the backscatter measurement (Fig. 28,) the ~180° scatter as described in chapter four is not entirely accurate. Taken over the whole front of the plastic array the backscatter angle ranges from 158-160°. These angles result in a difference of approximately 3-5keV from the calculated 180° backscatter deposit energy. Due to the low energy resolution of the plastics, this small difference in energy is not resolvable and therefore was not taken into account. The peaks in the plastic calibration (Fig. 29 and Fig. 30) were recorded as the total energy deposit for a 180° backscatter in every plastic.

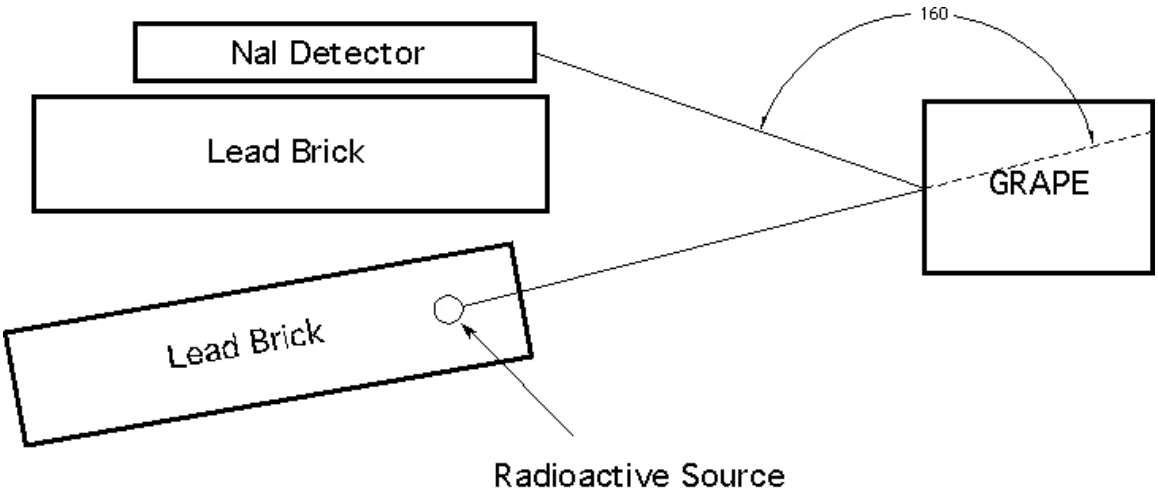

Figure 28: Schematic showing the setup for backscatter calibration.

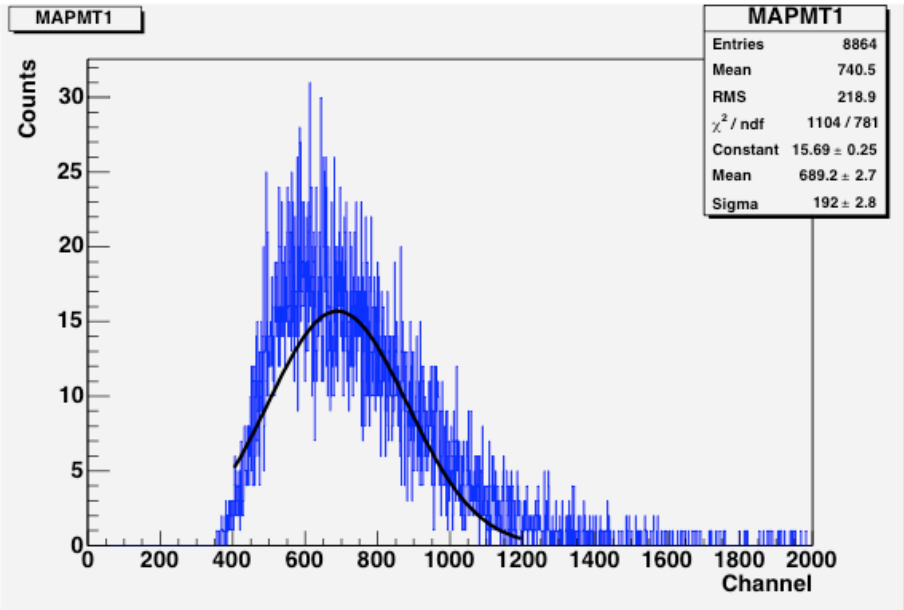

Figure 29: SM3 plastic calibration spectrum for a single plastic. Backscatter techniques were used to measure ^{57}Co.

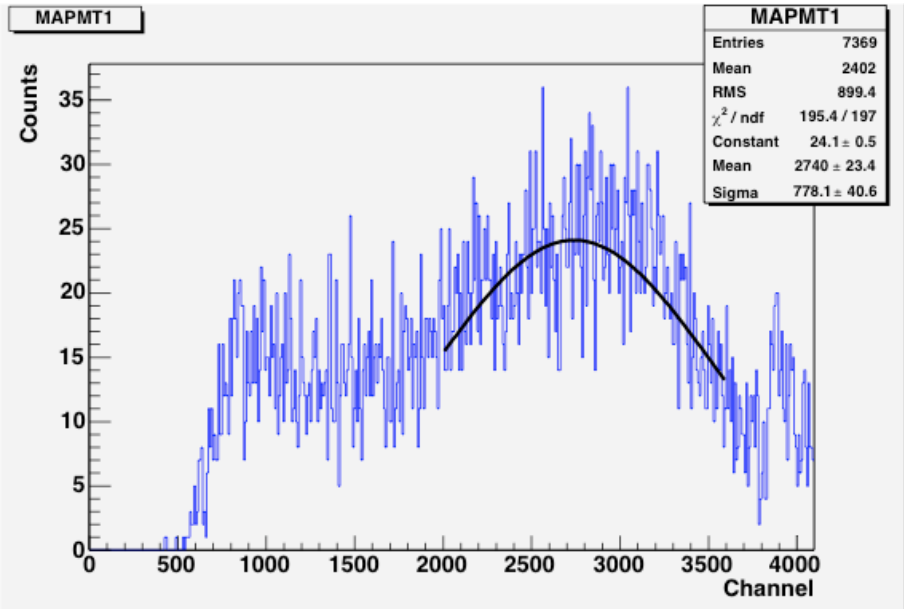

Figure 30: SM3 plastic calibration spectrum for a single plastic. Backscatter techniques were used to measure ^{133}Ba.

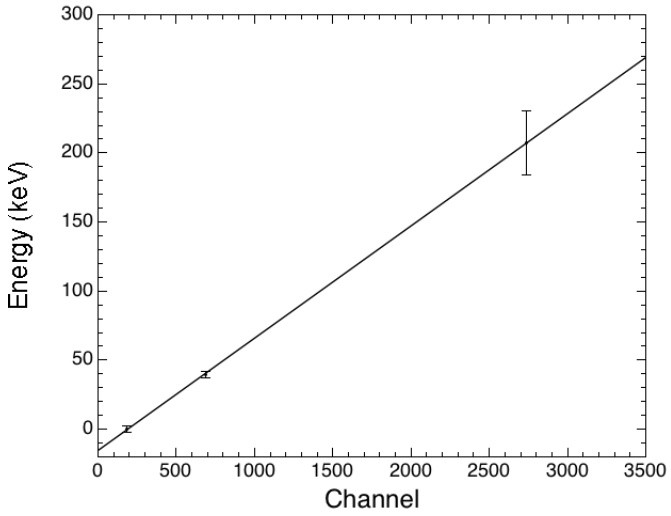

Figure 31: Energy vs. Channel plot used to determine plastic energy calibration.

SM3 Results

Initial laboratory tests of SM3 proved unsuccessful. It was discovered that there was significant optical cross-talk between the calorimeter and the twelve surrounding plastic elements. We believe that this can be attributed to the close proximity between the calorimeter and adjacent plastics. With a light output of ~4 times that of a plastic scintillator, the CsI(Na) calorimeter was contributing to the energy recorded in this inner plastic ring. This virtually eliminates our ability to reconstruct the kinematics of valid events. Initial investigation shows that it is possible for photons leaving the CsI(Na) to refract into adjacent plastic element anodes. With the cut away shown (Fig. 32) it is possible for photons exiting the CsI(Na) up to 1mm from the edge to be refracted into the plastic element anode. This only occurs for specific incident angles for photons leaving the CsI(Na), ~28.8-32.9° at the edge and ~32.4-32.9° at 1mm from the edge.

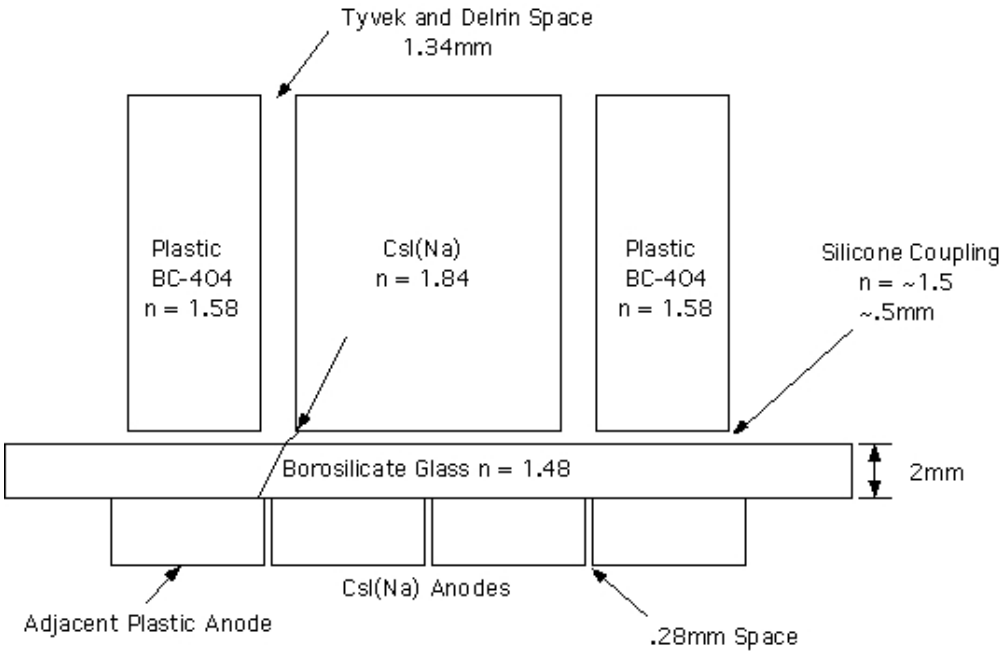

Figure 32: Cut away schematic of the CsI and surrounding plastics.

To correct for the cross-talk problem we decided to eliminate the inner twelve plastic scintillator elements from the analysis. This leaves 48 plastic elements in the array for analysis of the azimuthal scatter angle. The results reported in Fig. 33 represent the data collected with inner ring in place, but events occurring in the inner ring eliminated from the analysis. Data was collected for 0° and 90° polarization angle for ~4 days and yielded polarization levels of 56(±9)% and 55(±7)% respectively. Again simulations were used to obtain μ_{100} allowing us to determine these measured levels.

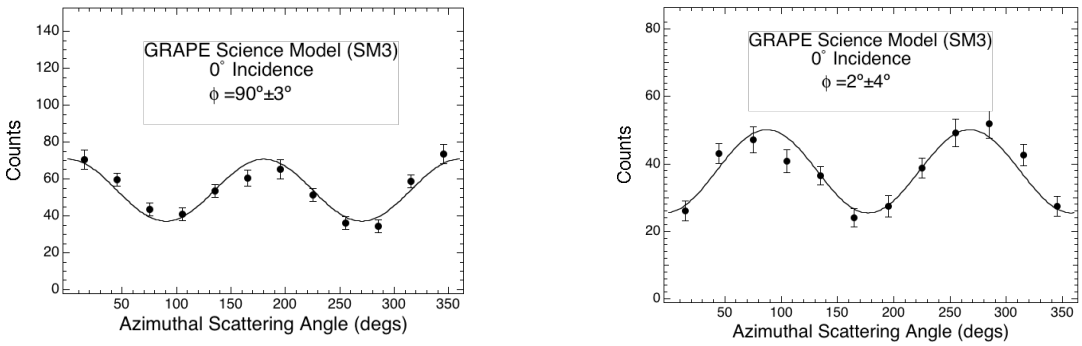

Figure 33: Results from SM3 with inner plastic ring eliminated.

Simulations

We have used simulations based on MGEANT (incorporating the GLEPS polarization code), discussed in chapter two, to model the response of the polarimeter to the experiment setup described in Chapter four. The simulation uses ^{137}Cs source located in the center of a lead brick and scattered through 90° before being incident on the polarimeter. The azimuthal scatter distribution seen in Fig. 34 represents the SM3 48 plastic element configuration. The simulated data yielded a modulation factor of 0.34(±)0.03 consistent with the measured modulation (0.32(±)0.04) for SM3 in the lab.

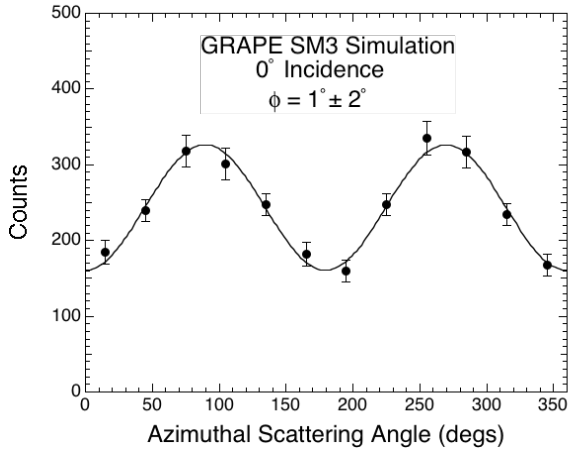

Figure 34: MGEANT simulated polarimeter experiment of SM3.

Further SM3 Testing

With the successful testing of SM3 nearing completion, the future of the GRAPE module looks promising. We first plan to further investigate the cross talk problem. The extent of possible light refraction into adjacent anodes needs to be investigated further. If it is found to be of minor significance than other potential problems need to be considered (i.e. improper spacing of elements leading to improper anode coverage.) Other important issues besides CsI(Na)-to-plastic cross talk is whether the problem also exists with the plastic elements as well and at what level. A detailed look at how well the Tyvek wrapping isolates the individual elements needs to be considered. If the plastic elements are not completely isolated optical cross talk becomes a potential issue.

Future plans include testing the SM3 with the inner ring of plastic scintillators removed. If cross talk issues cannot be resolved then it would be interesting to measure the impact of having the inactive inner ring in place. This should increase detector sensitivity by improving the statistics of valid events measured in polarized tests. By having the inner ring inactive we limit our ability to determine multiple scatters within

plastic elements. We also plan to test GRAPE at various incidence angles of incoming polarized radiation in order to determine sensitivity of the polarimeter to off-axis incident radiation.

Tests with a lower energy and polarization level have recently been conducted. A ^{137}Cs laboratory source was scattered through an angle of 120° within the polarizer before being incident on the polarimeter. This produces an initial beam of photons with an energy of ~225 keV and polarization level of ~30%. Our initial results look promising and as seen in Fig. 35 measured a polarization level of 29(±5)% for a ~5 day run.

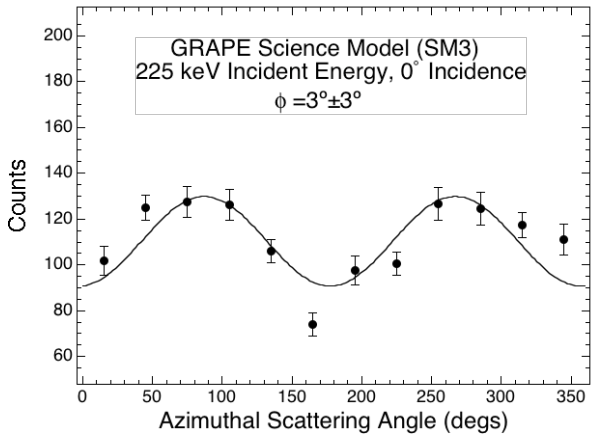

Figure 35: SM3 results using the ^{137}Cs source scattered through 120°.

A final consideration with SM3 is the threshold of the polarimeter. Tests have been conducted at the upper energy range of the design, but only as low as 225 keV. In order to measure polarization of incident radiation in the 50 keV range the low energy thresholds of the plastic elements needs to be ~4 keV. Currently the low energy thresholds of the plastic elements is ~27 keV, allowing GRAPE to be sensitive to incident

photons of ~150 keV. The current setup of SM3 has the capability of lowering the thresholds to ~15 keV allowing the polarimeter to be sensitive down to ~100 keV. Investigating ways to lower this threshold to provide sensitivity down to ~50 keV will also be included in further testing.

CHAPTER VI

FUTURE OF GRAPE

Science Model 4 (SM4)

The next step for GRAPE is improved coincidence timing and energy resolution. We plan to accomplish this by replacing the central CsI calorimeter with one based on Lanthanum Bromide ($LaBr_3$) [45]. This relatively new inorganic scintillator provides an energy resolution that is more than twice as good as NaI at 662 keV (3% vs. 7%). The $LaBr_3$ also provides for better timing characteristics. With decay times of ~25 nsec, it is comparable to the plastic scintillators used and will greatly improve the coincidence timing.

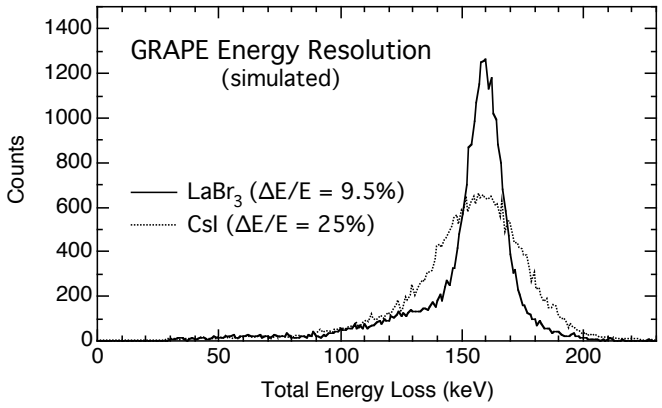

Figure 36: Simulated results showing the improved energy resolution of the SM4 design that would result from changing the CsI calorimeter to one made from $LaBr_3$.

GRAPE Deployment

Upon completion of SM4 testing we envision an engineering module (EM) of GRAPE that will be suitable as a piggyback mission on a balloon flight. The EM will consist of a 2×2 array of MAPMT modules all packaged within a thermally controlled housing that includes the necessary supporting electronics (HV circuitry, signal processing electronics, etc.) [9]. Each of the four modules will be independently calibrated as described earlier prior to being integrated into the array. With the array completely assembled, a combined calibration of the EM will be completed. In order to reduce background the entire EM will be surrounded by a plastic anticoincidence shield.

An ideal balloon mission would be a Continental United States (CONUS) balloon flight launched from Ft. Sumner or Palestine during the fall of 2006. Due to the limited size of the array we do not expect to return any significant science from the flight, but do expect to evaluate the GRAPE design operating characteristics in a relevant environment. We hope to gain an insight of the instrumental background and mechanical integrity of the design, particularly the ruggedness of the MAPMT H8500. If the ruggedness of the H8500s becomes an issue we have also explored the use of more rugged MAPMTs, such as the R5900. The EM will also be our first opportunity to test the designs response to events that are scattered between different detector modules. This will become part of the laboratory calibrations,

One long-term option for GRAPE would be as a primary instrument on an Ultra-Long Duration Balloon (ULDB) payload. The ULDB technology is expected to provide flight durations of approximately 100 days. We would expect a 1 m^2 array of GRAPE modules to easily fit within the envelope of a ULDB payload. A second long-term option of GRAPE would be as a spacecraft payload attached to the International Space Station or as a small satellite platform.

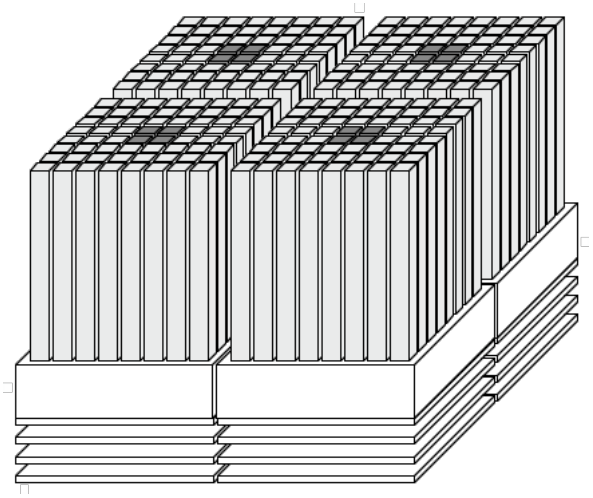

Figure 37: An array of four GRAPE modules.

CHAPTER VII

CONCLUSIONS

The SM2 and SM3 modules have demonstrated the effectiveness of the GRAPE MAPMT design. We have measured polarization levels in both models that are in agreement with the predicted laboratory results. We have also shown that the measurements are also in agreement with the simulated results on MGEANT using the GLEPS extension.

GRAPE has the ability to measure the polarization levels of emitted gamma-rays from solar flares and GRBs and provide important clues to the emission mechanisms and source geometries. The history of polarimetric measurements has been met with much difficulties and speculation. The most recent measurements conducted with RHESSI point to the need for a dedicated polarimeter sensitive in the gamma-ray regime. The continued development of GRAPE will produce a flyable instrument to meet these needs.

LIST OF REFERENCES

[1] Lei, F., Dean, A.J., & Hills, G.L. 1997, Sp. Sci. Rev., 82, 309. *Compton Polarimetry in Gamma-Ray Astronomy.*

[2] McConnell, M.L., et al., 1998b, in AIP Conf. Proc. 428, "Gamma-Ray Bursts", eds. C.A. Meegan, R.D. Preece, & T.M. Koshut (New York: AIP), 889. *The Development of a Hard X-Ray Polarimeter for Gamma-Ray Bursts.*

[3] McConnell, M.L., Macri, J., McClish, M., Ryan, J., Forrest, D.J. & Vestrand, W.T. 1999a, IEEE Trans. Nucl. Sci., 46(4), 890. *The Development of a Hard X-Ray Polarimeter for Astrophysics.*

[4] McConnell, M.L., Macri, M., McClish, M., & Ryan, J. 1999b, 26th Internat. Cosmic Ray Conf., 6, 21. *A Polarimeter for Studying Hard X-Rays from Solar Flares.*

[5] McConnell, M.L., Macri, M., McClish, M., & Ryan, J. 1999c, Proc. SPIE, 3764, 70. *Recent Laboratory Tests of a Hard X-Ray Solar Flare Polarimeter.*

[6] McConnell, M.L., Macri, J.R., McClish, M., & Ryan, J.M. 2000, in ASP Conf. Ser. 206, "High Energy Solar Physics: Anticipating HESSI," eds. R. Ramaty and N. Mandzhavidze (San Francisco, ASP), 280. *A Modular Hard X-Ray Polarimeter for Solar Flares.*

[7] McConnell, M.L., Ledoux, J.R. Macri, J.R. & Ryan, J.M., 2002a, SPIE Conf. Proc., 4851. *A Hard X-ray Polarimeter for Gamma-Ray Bursts and Solar Flares.*

[8] McConnell, M.L., Ledoux, J., Macri, J.R., & Ryan, J.M., 2003, AIP Conf. Proc. 662, Gamma-Ray Burst and Afterglow Astronomy (New York: AIP), 503. *The Development of GRAPE, A Gamma-Ray Polarimeter Experiment.*

[9] McConnell, M.L., Ledoux, J.R. Macri, J.R. & Ryan, J.M. 2003, SPIE *Conf. Proc.*, 5165. *Dedicated Polarimeter Design for Hard X-Ray and Soft Gamma-Ray Astronomy.*

[10] McConnell, M.,L., Smith, D.M., Emslie, A.G., Hurford, G.J., Lin, R.P., & Ryan, J.M. 2003b, BAAS, 35 (2), 616. *Measuring Hard X-Ray Polarization of Solar Flares with RHESSI.*

[11] Piran, T. 1999, Phys. Rept., 314, 575. *Gamma-Ray Bursts and the Fireball Model.*

[12] Hurley, K., Sari, R., & Djorgovski, S.G., 2003, astro-ph/0211620. *Cosmic Gamma-Ray Bursts, Their Afterglows and Their Host Galaxies.*

[13] Strong, I. B. et al., 1973, Los Alamos Conf. On Transient Cosmic Gamma and X-Ray sources, unpublished.

[14] Costa, E., Frontera, F., Heise, J. et al., 1997, Nature **387**, 783.

[15] Eichler, D., Livio, M., Piran, T., & Schramm, D. 1989, Nature, 340, 126. *Nucleosynthesis, Neutrino Bursts and Gamma Rays from Coalescing Neutron Stars.*

[16] Woosley, S. 1993, Ap. J., 405, 273. *Gamma-Ray Bursts from Stellar Mass Accretion Disks around Black Holes.*

[17] Paczynski, B. 1998, in AIP Conf. Proc. 428, "Gamma-Ray Bursts", eds. C.A. Meegan, R.D. Preece, & T.M. Koshut (New York: AIP), 783. *Gamma-Ray Bursts as Hypernovae.*

[18] Covino, S., et al. 1999, A&A, 348, L1. GRB 990510: *Linearly Polarized Radiation from a Fireball.*

[19] Bersier, D., et al. 2003, Ap. J., 583, L63. *The Strongly Polarized Afterglow of* GRB 020405.

[20] Covino, S., Ghisellini, G., Lazzati, D., & Malesani, D. 2003, astro-ph/0301608. *Polarization of Gamma-Ray Burst Optical and Near-Infrared Afterglows.*

[21] Gruzinov, A. 1999, Ap. J., 525, L29. *Strongly Polarized Optical Afterglows of Gamma-Ray Bursts.*

[22] Gruzinov, A., &Waxman, E. 1999, Ap. J., 511, 852. *Gamma-Ray Burst Afterglow: Polarization and Analytic Light Curves.*

[23] Sari, R. 1999, Ap. J., 524, L43. *Linear Polarization and Proper Motion in the Afterglow of Beamed Gamma-Ray Bursts.*

[24] Ghisellini, G., & Lazzati, D. 1999, MNRAS, 309, L7. *Polarization LightCurves and Position Angle Variation of Beamed Gamma-Ray Bursts.*

[25] Coburn, W. & Boggs, S. 2003, Nature, 423, 415. *Polarization of the prompt Gamma-Ray emission from the Gamma-Ray burst of 6 December 2002.*

[26] McConnell, M.L., Ryan, J.M., Smith, D.M., Lin, R.P., & Emslie, A.G., 2002, Solar Phys., 210, 125. *RHESSI as a Hard X-Ray Polarimeter*.

[27] Brown, J.C. 1972, Solar Phys., 26, 441. *The Directivity and Polarisation of Thick Target X-Ray Bremsstrahlung from Solar Flares*.

[28] Langer, S.H., & Petrosian, V. 1977, Ap. J., 215, 666. *Impulsive Solar X-Ray Bursts. III. Polarization, Directivity, and Spectrum of the Reflected and Total Bremsstrahlung Radiation from a Beam of Electrons Directed Towards the Photosphere*.

[29] Bai, T., & Ramaty, R. 1978, Ap. J., 219, 705. *Backscatter, Anisotropy, and Polarization of Solar Hard X-Rays*.

[30] Emslie, A.G., & Vlahos, L. 1980, Ap. J., 242, 359. *Radiation Signatures from a Locally Energized Flaring Loop*.

[31] Leach, J., & Petrosian, V. 1983, Ap. J., 269, 715. *The Impulsive Phase of Solar Flares. II. Characteristics of the Hard X-Rays*.

[32] Zharkova, V.V., Brown, J.C., & Syniavskii, D.V. 1995, Astron. Astrophys., 304, 284. *Electron Beam Dynamics and Hard X-Ray Bremsstrahlung Polarization in a Flaring Loop with Return Current and Converging Magnetic Field*.

[33] Charikov, Ju.E., Guzman, A.B., & Kudryavtsev, I.V. 1996, Astron. Astrophys., 308, 924. *Hard X-Ray Emission of Solar Flares and Non-Stationary Kinetics of Electron Beams*.

[34] Chanan, G.A., Emslie, A.G., & Novick, R. 1988, Solar Phys., 118, 309. *Prospects for Solar Flare X-Ray Polarimtery*.

[35] Tindo, I.P., Ivanov, V.D., Mandel'stam, S.L., & Shuryghin, A.I. 1970, Solar Phy., 14, 204. *On the Polarization of the Emission of X-Rays from Solar Flares*.

[36] Nakada, M.P., Neupert, W.M., & Thomas, R.J. 1974, Solar Phy., 37, 429. *Polarization Results of Solar X-Rays from OSO-7*.

[37] Tindo, I.P., Shuryghin, A.I., & Steffen, W. 1976, Solar Phy., 46, 219. *The Polarization of X-Ray Emission of Some Solar Flares in July 1974*.

[38] Tramiel, L.J., Channan, G.A., & Novick, R., 1984, Ap. J., 280, 440. *Polarization Evidence for the Isotropy of Electrons Responsible for the Production of 5-20 keV X-Rays in Solar Flares*.

[39] McConnell, M.L., Smith, D.M., Hurford, G.J., Fivian, M., Lin, R.P, Emslie, A.G., 2006, to be published in Solar Physics. *RHESSI Measurements of Hard X-Ray Polarization from Solar Flares*.

[40] Smith, D.M., et al., 2002, Solar Physics, 210, 33. *The RHESSI Spectrometer*.

[41] Costa, E., Cinti, M.N., Feroci, M., Matt, G., & Rapisarda, M. 1993, Proc. SPIE, 2010, 45. *Scattering Polarimetry for X-Ray Astronomy by Means of Scintillating Fibers*.

[42] Novick, R. 1975, Sp. Sci. Rev., 18, 389. *Stellar and Solar X-Ray Polarimetry*.

[43] McConnel, M.L., Kippen, R.M, 2004, AAS-HEAD Meeting, poster. *The GLEPS Package for SimulatingPolarized Gamma Rays with GEANT3*.